Nano Research Energy

ISSN 2791-0091 CN 10-1944/O6
https://doi.org/10.26599/NRE.2026.9120276

Research Article

Upcycling Spent Graphite into Fast-Charging and Sustainable Anodes via Interfacial Catalytic-Percolative Engineering

Xueqian Li[1,§], Xiaodong Zhang[1,§], Jiao Lin[1], Jiahui Lu[2], Yushuo Zhang[2], Qingrong Huang[1], Mengyao Liu[2], Meng Xu[2], Renjie Chen[1,3,4], Yi Zhao[2,3](✉), Li Li[1,3,4](✉)

[1] Beijing Key Laboratory of Environmental Science and Engineering, School of Materials Science and Engineering, Beijing Institute of Technology, Beijing 100081, China

[2] State Key Laboratory of Chemical Engineering, College of Chemistry, Beijing University of Chemical Technology, Beijing 100029, China

[3] Shandong Key Laboratory of Advanced Chemical Energy Storage and Intelligent Safety, Advanced Technology Research Institute, Beijing Institute of Technology, Jinan 250300, China

[4] Innovative Research Team in High-Safety Energy Storage System and Smart Microgrids of Guangdong Province, Beijing Institute of Technology (Zhuhai), Zhuhai 519088, China

[§] Xueqian Li and Xiaodong Zhang contributed equally to this work.

Nano Research Energy, **Just Accepted Manuscript** • https://doi.org/10.26599/NRE.2026.9120276
https://www.sciopen.com/journal/2791-0091 on Sep. 17, 2026

© The Authors(s)

Just Accepted

This is a "Just Accepted" manuscript, which has been examined by the peer-review process and has been accepted for publication. A "Just Accepted" manuscript is published online shortly after its acceptance, which is prior to technical editing and formatting and author proofing. Tsinghua University Press (TUP) provides "Just Accepted" as an optional and free service which allows authors to make their results available to the research community as soon as possible after acceptance. After a manuscript has been technically edited and formatted, and the page proofs have been corrected, it will be removed from the "Just Accepted" web site and published officially with volume and article number (e.g., Nano Research Energy, 2025, 4, e9120191). Please note that technical editing may introduce minor changes to the manuscript text and/or graphics which may affect the content, and all legal disclaimers that apply to the journal pertain. In no event shall TUP be held responsible for errors or consequences arising from the use of any information contained in these "Just Accepted" manuscripts. To cite this manuscript please use its Digital Object Identifier (DOI®), which is identical for all formats of publication.

TABLE OF CONTENTS (TOC)

Upcycling Spent Graphite into Fast-Charging and Sustainable Anodes via Interfacial Catalytic-Percolative Engineering

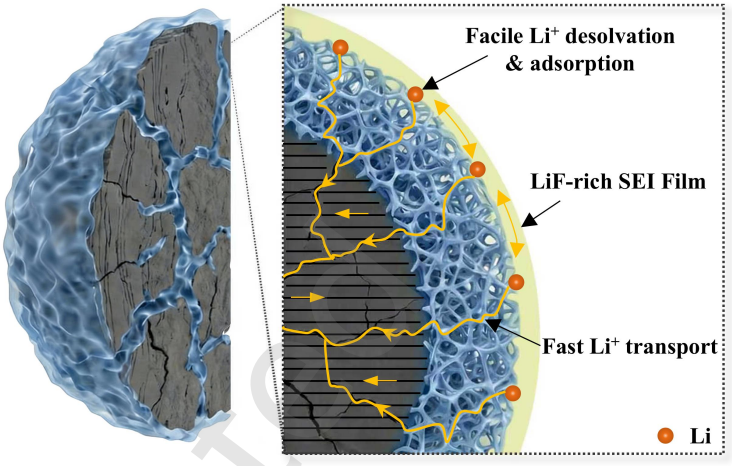
Xueqian Li [1,§], Xiaodong Zhang [1, §], Jiao Lin [1], Jiahui Lu [2], Yushuo Zhang [2], Qingrong Huang [1], Mengyao Liu [2], Meng Xu [2], Renjie Chen [1, 3, 4], Yi Zhao [2, 3, *], and Li Li [1, 3, 4, *]

[1] Beijing Institute of Technology, China

[2] Beijing University of Chemical Technology, China

[3] Advanced Technology Research Institute, Beijing Institute of Technology, China

[4] Beijing Institute of Technology (Zhuhai), China



Herein, we present a catalytic-percolative interfacial engineering strategy to upcycle spent graphite by constructing an amorphous Al_2O_3 nanonetwork on regenerated graphite, delivering robust structural stability, accelerated fast-charging kinetics, and high reversible capacity.

Just Accepted

Nano Research Energy

ISSN 2791-0091 (print); 2790-8119 (online)
https://doi.org/10.26599/NRE.2026.9120276

Research Article

Upcycling Spent Graphite into Fast-Charging and Sustainable Anodes via Interfacial Catalytic-Percolative Engineering

Xueqian Li [1,§], Xiaodong Zhang [1, §], Jiao Lin [1], Jiahui Lu [2], Yushuo Zhang [2], Qingrong Huang [1], Mengyao Liu [2], Meng Xu [2], Renjie Chen [1, 3, 4], Yi Zhao [2, 3] (✉), and Li Li [1, 3, 4] (✉)

[1] *Beijing Key Laboratory of Environmental Science and Engineering, School of Materials Science and Engineering, Beijing Institute of Technology, Beijing 100081, China*
[2] *State Key Laboratory of Chemical Engineering, College of Chemistry, Beijing University of Chemical Technology, Beijing 100029, China*
[3] *Shandong Key Laboratory of Advanced Chemical Energy Storage and Intelligent Safety, Advanced Technology Research Institute, Beijing Institute of Technology, Jinan 250300, China*
[4] *Innovative Research Team in High-Safety Energy Storage System and Smart Microgrids of Guangdong Province, Beijing Institute of Technology (Zhuhai), Zhuhai 519088, China*
[§] *Xueqian Li and Xiaodong Zhang contributed equally to this work.*

© The Author(s) 2026
Received: 14 July 2026 / **Revised:** 31 August 2026 / **Accepted:** 13 September 2026 (已核对)

ABSTRACT

Driven by the urgent requirements for sustainable lithium-ion batteries, the re-utilization of spent graphite featuring accumulated defects and interfacial degradation is shifting from simple compositional recovery toward functional reconfiguration. Herein, an effective interfacial strategy is proposed to upcycle spent graphite into recycled graphite encapsulated by amorphous Al_2O_3 nanonetworks (denoted as ARG) *via* a facile low-temperature heat treatment. According to experimental and theoretical calculation results, the amorphous Al_2O_3 coating containing Lewis-acidic Al^{3+} sites can strongly interact with electrolytic solvent molecules to reduce the Li^+ desolvation energy barrier, catalyzing the formation of a LiF-rich SEI layer with improved electronic conductivity and reduced interfacial charge transfer resistance. Moreover, thin Al_2O_3 interphase, featuring negative Li^+ adsorption energy, couples effectively with inherent bulk defects, thereby enabling substantially enhanced Li^+ trapping and storage via multidimensional ion diffusion pathways. Contributing to the interfacial "catalytic-percolative" regulation, ARG anode exhibits an ultra-high capacity (394 mAh g^{-1}), superior rate performance and excellent cycling stability even at 4 C, providing novel insights into constructing fast-charging and durable upcycled graphite with significant economic and ecological value.

KEYWORDS

spent lithium-ion batteries, upcycling graphite, interfacial modification engineering, fast-charging capability, improved structural stability

1 Introduction

With the rapid development of the global electric vehicle industry, an inevitable retirement wave of lithium-ion batteries (LIBs) with limited service life of 5-8 years is set to emerge in the coming few years [1-3]. Therefore, the sustainable reuse and recycling of spent battery materials is essential for alleviating environmental burdens and forming the strategic core of a closed-loop industrial chain [4]. As one of the key battery materials, accounting for 10~20% of the total mass, high-grade graphite faces ever-growing annual demand to address the foreseeable supply shortage [5, 6]. Based on this, the high-efficiency recycling of spent graphite (SG) becomes the research hotspot to avoid the energy-intensive production process, thereby enabling sustainable and economic LIBs. It is worth noting that traditional pyrometallurgy and hydrometallurgy generally focus on the purification and separation of metal components, rather than the *in situ* repair and microstructural reconstruction of spent LIBs [7]. Therefore, recycled graphite (RG) retains structural defects and interface degradation, resulting in inferior rate capability and severe capacity decline during long-term cycling, especially under fast charging conditions [8]. Specifically, the directly regenerated RG still faces the issues of structural distortion and stress accumulation at the graphite lattice during repeated Li^+

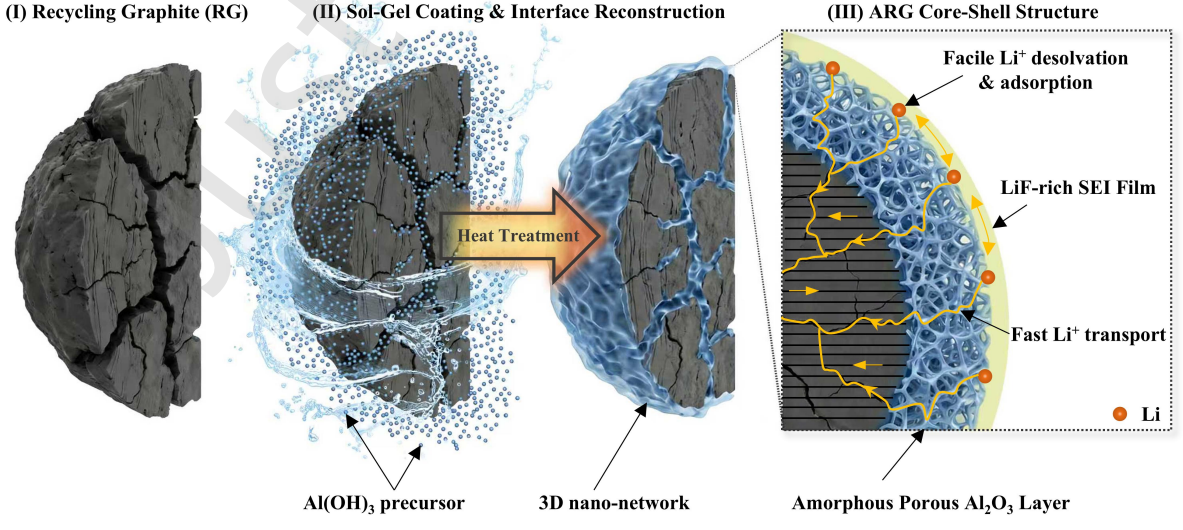
© The Author(s) 2026. Published by Tsinghua University Press. The articles published in this open access journal are distributed under the terms of the Creative Commons Attribution 4.0 International License (http://creativecommons.org/licenses/by/4.0/), which permits use, distribution and reproduction in any medium, provided the original work is properly cited.

Address correspondence to Yi Zhao, zybattery@buct.edu.cn; Li Li, Lily863@bit.edu.cn

Just Accepted

insertion/extraction, manifested as abnormal expansion of the lattice spacing and the formation of microcracks. More critically, the continuous electrolyte decomposition typically leads to the formation of a thick and uneven solid electrolyte interphase (SEI) layer, which blocks ion diffusion pathways, resulting in increased charge transfer resistance and sluggish interfacial kinetics [9]. Therefore, exploring effective upcycling strategies to reconstruct SEI layer and enhance interfacial reaction kinetics is essential yet remains a challenge for achieving fast-charging, durable graphite anodes.

Current research on SG recycling has evolved from resource extraction to deep functional reconfiguration for upcycled graphite materials through interface reformation. Besides the initial restoration of SG, most of the traditional recycling processes fail to address the sluggish Li^+ transport and microstructural damage of regenerated graphite after long-term battery cycling [10]. More importantly, the slow Li^+ desolvation process and high interface impedance severely limit the fast-charging performance of RG under high-rate charging/discharging. To address these issues, surface modification approaches have been widely explored to reconstruct interface between graphite and electrolyte for improved interfacial dynamics and a robust SEI layer of RG materials [11-15]. For example, building a carbon coating on regenerated graphite by utilizing external carbon precursors (such as sucrose) effectively enhanced the electrical conductivity and partially repaired structural defects in SG [15]. However, under high current density conditions, the dense amorphous carbon layer significantly increases the tortuosity of ion diffusion pathways, thus impeding rapid Li^+ transmission, and eventually resulting in rapid capacity fade [16]. Recently, Da *et al.* used a low-temperature polymerization method to coat a methyl methacrylate (PMMA) layer onto SG surface as an artificial SEI film, which remarkably heals surface defects and suppressed electrolyte decomposition for improved stability of recycled graphite [11]. Nevertheless, such organic coating layers typically lack catalytic activity for accelerating Li^+ desolvation and diffusion kinetics, thus preventing the application of fast-charging LIBs at high current densities. In contrast, metal oxide layers (e.g., Al_2O_3, TiO_2, SnO_2) are regarded as effective in regulating the interfacial chemical environment and promoting Li^+ storage behaviors, owing to their excellent structural stability and lithium ion adsorption capacity [17-19]. Among them, Al_2O_3 has attracted considerable attention for graphite interface protection owing to its excellent chemical stability, mechanical strength, and ability to inhibit electrolyte side reactions [20-22]. Via atomic layer deposition (ALD) technique, an ultra-thin Al_2O_3 coating with precisely controllable thickness can be fabricated on the graphite surface, which effectively stabilizes the graphite-electrolyte interface and forms uniform SEI layer [23, 24]. However, the high manufacturing cost and low deposition efficiency of the ALD process limit its application potential in large-scale regeneration of spent graphite anodes [20]. Furthermore, the dense Al_2O_3 layer with poor ion diffusion tunnels fails to cooperate with intrinsic defects of degraded graphite, thereby blocking Li^+ diffusion pathways along with increased interfacial resistance to deteriorate the rate performance of RG [25]. Therefore, reconstructing an effective inorganic interface with excellent ion permeability and stability on defect-rich repaired graphite substrate is critical for transforming SG into fast-charging, durable RG anodes.



Scheme 1. Schematic illustration of fabricating fast-charging and durable ARG *via* a feasible low-temperature heat treatment method.

Herein, we design an amorphous alumina nanonetwork uniformly wrapped onto the surface of RG (denoted as ARG), to upgrade SG through facile sol-gel coating and low-temperature heat treatment (**Scheme 1**). Benefiting from the dual "catalytic-percolation" function of the Al_2O_3 layer, the ARG anode effectively catalyzes Li^+ desolvation and enhances interfacial ion diffusion kinetics, thereby breaking the fast-charging kinetic bottleneck of most reported regenerated graphite. Combined experimental and theoretical analyses indicate that the Lewis acidic Al^{3+}

Just Accepted

sites within the amorphous alumina can interact strongly with electrolyte solvent molecules, thus lowering the Li^+ desolvation energy barrier and facilitating the formation of a LiF-rich SEI to improve interfacial stability and charge transfer kinetics. In addition, the thin but porous Al_2O_3 interface featured with negative Li^+ adsorption energy can further interconnect with inherent defects of bulk graphite to trap and store more Li^+ ions for multi-dimensional ion diffusion pathways, endowing ARG anode with a super theoretical capacity of 394 mAh g^{-1} at 0.1 C. Contributing to the synergistic regulation Al_2O_3 interface, ARG anode exhibits a high-rate performance of 366 mAh g^{-1} and 236 mAh g^{-1} at 1 C and 4 C, respectively, while maintaining excellent cycling stability. This study provides an effective interfacial reformation strategy for upcycling SG into fast-charging and stable ARG with significant economic and ecological value.

2 Results and discussion

Regenerated ARG with a uniform Al_2O_3 interfacial coating was fabricated to construct a multidimensional ionic infiltration network for fast-charging and sustainable graphite anodes. During the targeted restored process, the morphological and compositional variations of SG supplied a detailed elucidation for upcycled ARG with interfacial regeneration. According to scanning electron microscopy (SEM) images of commercial graphite (CG) and SG, most metal and electrolytic impurities have been removed from the surface of RG after chemical purification and low-temperature heat treatment (**Fig. S1**). However, RG still exhibits obvious cracks and microscopic defects caused by repeatable lattice shrinkage/expansion and disassembly during long-term battery cycling. In contrast, ARG exhibits a more uniform morphology, with the surface completely covered by ultrathin, porous Al_2O_3 nanosheets (**Fig. S2**). The transmission electron microscopy (TEM) images clearly reveal that core-shell ARG displays well-restored graphite crystals and a uniform alumina coating with a thickness of ~10 nm (**Fig. 1a**). Notably, the surface graphite of ARG shows diverse interlayer spacing caused by the intrinsic cracks inherited from spent graphite. Within the bulk region, the bulk graphite of ARG maintains the typical long-range ordered structure with a slightly higher $d_{(002)}$ crystal plane spacing of 0.3358 nm than that of CG, indicating the hierarchical structure of regenerated ARG for accelerated Li^+ diffusion (**Fig. 1b**). Moreover, the selected area electron diffraction (SAED) patterns of ARG merely display three distinct concentric rings assigned to (002), (100) and (110) planes of graphite substrate (**Fig. 1c**). The absence of characteristic diffraction rings for crystalline alumina, along with the diffuse halo background, verifies the amorphous nature of the Al_2O_3 coating layer. To confirm structural variations of ARG, X-ray diffraction (XRD) results show that ARG retains all characteristic diffraction peaks of hexagonal graphite (JCPDS 00-056-0160) without any other peaks during the regeneration process, further confirming the well-preserved layered crystalline structure of bulk graphite wrapped by amorphous Al_2O_3 coating in ARG (**Fig. 1d**). According to the Bragg formula, the evolution of the $d_{(002)}$ spacing further reveals the structural recovery transformation of SG upcycling to ARG. Specifically, the interlayer spacing of ARG decreases from 0.3364 nm (RG) to 0.3358 nm, slightly higher than that of CG (0.3356 nm), induced by the residual defects and cracks in regenerated graphite surface even after the interface constraint of the Al_2O_3 layer. As shown in the Raman spectra, the intensity ratio of the D-band (1352 cm^{-1}, sp^3-type disordered carbon) to the G-band (1582 cm^{-1}, sp^2-type ordered carbon) can be utilized to determine the characterize the graphitization degree [26]. The I_D/I_G ratios of ARG, RG and CG are 0.26, 0.12 and 0.08, respectively (**Fig. 1e**). The elevated I_D/I_G ratio of ARG indicates an increased degree of surface disorder, which facilitates SEI reconstruction and provides additional active sites for Li^+ storage. To further examine the structural and compositional evolution of the ARG surface, X-ray photoelectron spectroscopy (XPS) and TEM characterization were conducted (**Fig. S3**). Besides the presence of elemental Al, high-resolution O 1*s* and C 1*s* XPS spectra reveal that the dominant peaks of C-O, C=O, and C-OH groups in CG and RG are disrupted by the introduction of Al-O groups originating from the amorphous Al_2O_3 layer within ARG. Furthermore, the Al 2*p* spectrum of ARG shows an Al-O-H peak at 75.5 eV, re-confirming the successful coating of Al_2O_3 onto restored graphite surface for additional Li^+ adsorption and storage sites (**Fig. 1f**) [27]. The inductively coupled plasma optical emission spectrometry (ICP-OES) further confirms effective recovery of Li, Cu, and Mn from SG, and the Al content of ~1.28 wt% in ARG (**Table S1**). Moreover, TEM-elemental mapping images directly reveal the uniform alumina layer on the graphite surface, verifying the core-shell structure of ARG (**Fig. 1g**) [28]. Therefore, amorphous Al_2O_3 coating uniformly reshapes the graphite interface via Lewis acid-base interaction and defect-oxide synergy with graphite, significantly catalyzing Li^+ desolvation process and boosting its migration rate for improved fast-charging capability and suppressed Li segregation of ARG.

To optimize the Al_2O_3 loading, the electrochemical performance of ARG with different $Al(NO_3)_3{\cdot}9H_2O$ precursor addition was measured in graphite||Li half cells. The results show that the ARG-5 electrode exhibits the highest initial capacity and superior rate capability compared to ARG-1 and ARG-10, which was chosen as the optimal ARG in the following battery tests (**Fig. S4**). The initial three-cycle cyclic voltammetry (CV) curves of the three typical graphite anodes were measured at 0.1 mV s^{-1} within 0.01 ~ 2.0 V (*vs.* Li/Li^+). During the first discharge, the irreversible reduction peak at 0.68 V is attributed to

Just Accepted

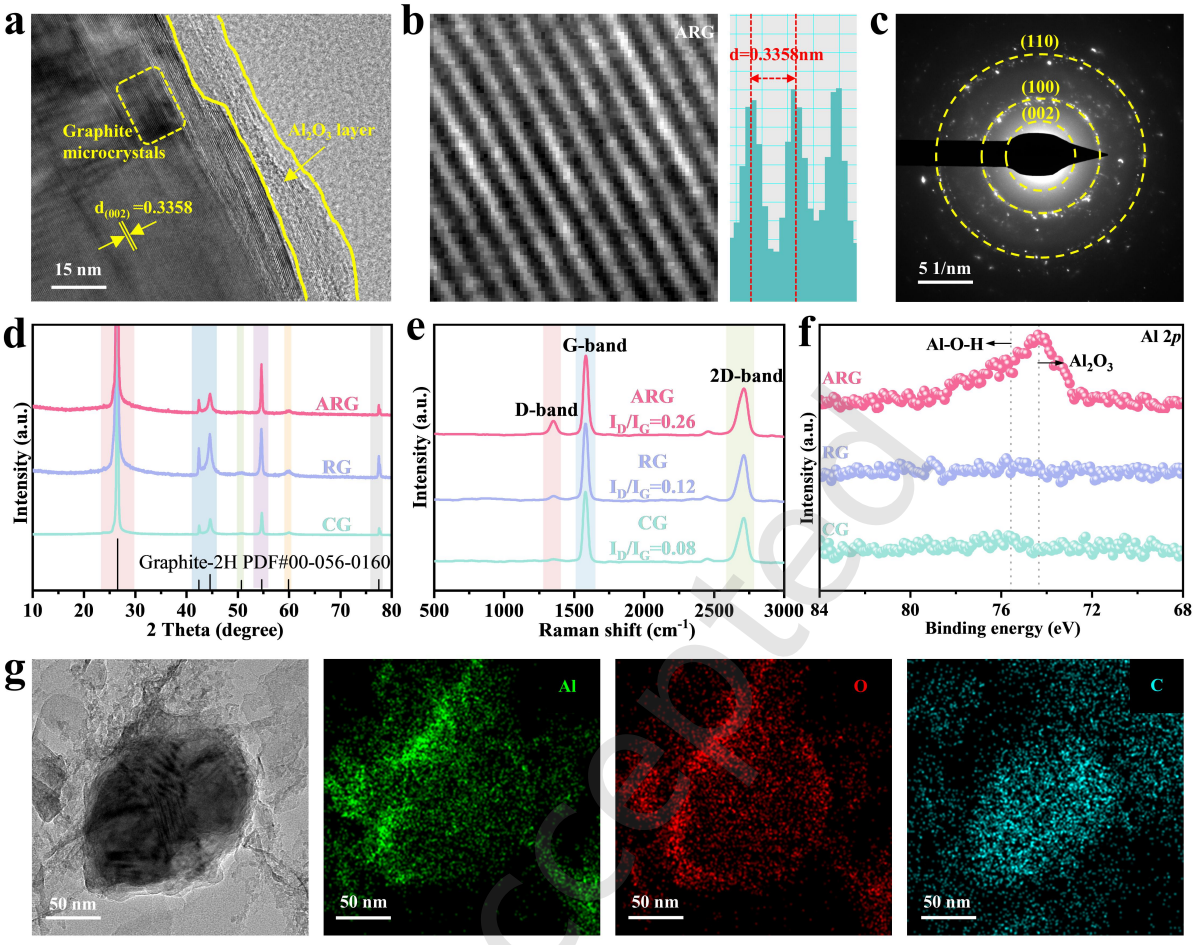


Fig. 1. Morphological and structural-compositional characterizations of ARG, RG, and CG anodes. (a) HRTEM images of ARG. (b) The lattice fringes of ARG. (c) SAED patterns of ARG. (d) XRD patterns of the ARG, RG and CG. (e) Raman spectra of the ARG, RG, and CG. (f) Al 2*p* spectra of the ARG, RG, and CG electrodes. (g) TEM-elemental desperation mapping images of ARG.

electrolyte decomposition and formation of the SEI film (**Fig. 2a**) [29]. Notably, two reduction peaks and one oxidation peak appear around 0.18/0.07 V and 0.2 V, respectively, in the subsequent two cycles, which are induced by the Li^+ insertion/extraction process [30]. Furthermore, the redox peaks and integral CV area of ARG are more coincident and higher than those of RG and CG anodes, indicating the reversible phase transition of LiC_{24} ↔ LiC_{18} ↔ LiC_{12} ↔ LiC_6 along with enhanced Li^+ storage capability attributed to the interfacial modification of Al_2O_3 coating (**Figs. S5**, **S6**). Compared with RG and CG, the galvanostatic charge-discharge (GCD) curve of ARG electrode delivers the highest discharge capacity of 477.1 mAh g^{-1} at 0.1C (1 C = 372 mA g^{-1}), exceeding the CG and RG (420.9 and 449.8 mAh g^{-1}, respectively), which can be attributed to the optimized Al_2O_3 coating with additional Li^+ adsorption and storage sites (**Fig. S7**) [31]. Moreover, ARG electrode retains significantly higher capacity retention of 329.49 and 238.52 mAh g^{-1} at high rates of 2C and 4C, respectively, than that of RG (only 204.11 and 98.78 mAh g^{-1}) and CG (mere 278.68 and 168.77 mAh g^{-1}), which could be ascribed to the reconstructed Al_2O_3 interface with boosted charge diffusion kinetics for fast-charging characteristic (**Figs. 2b**, **S8**, **S9**). The systematic comparison of the initial discharge capacity and initial coulombic efficiency (ICE) further indicates the outstanding Li^+ storage capability and modulated SEI composition of ARG electrode induced by the initial minor irreversible reaction between protective Al_2O_3 layer and organic electrolytes (**Fig. S10**) [32]. According to the rate performance results, ARG electrode exhibits specific discharge capacities of 394, 383, 366, 329, and 236 mAh g^{-1} at 0.1, 0.5, 1, 2, and 4 C, respectively, obviously higher than those of RG and CG electrodes (**Fig. 2d**). When the current density gradually returns to 0.1 C, ARG electrode nearly recovers its initial capacity, proving the durability of the reconstructed SEI with boosted charge transport and ion diffusion rates for fast-charging ARG||Li batteries. Besides, ARG electrode also demonstrates excellent cycling stability with a high capacity retention rate of 98.21% after 100 cycles at 1 C, superior to that of CG (88.06%) and RG (85.09%), respectively, proving the positive effect of Al_2O_3 interface for improved structural stability and suppressed side reactions associated with lithium evolution (**Fig. 2c**). Additionally, the ARG maintains high specific capacities of 285.2 and 160.7 mAh g^{-1} after 200 cycles at 2 C and 4 C, respectively (**Fig. 2e**). In contrast, the RG electrode experiences a significant

Just Accepted

capacity drop to 29.2 and 19.3 mAh g^{-1} after 200 and 300 cycles, respectively, at 4 C, re-confirming the significant role of Al_2O_3 coating in regulating surface chemistry of ARG for rapid Li^+ diffusion and fast-charging ability (**Fig. S11**). More details of the GCD profiles for RG and ARG are carefully collected after different cycles at 4C, highlighting the superb durability of restored graphite reconstructed by amorphous Al_2O_3 (**Fig. S12**). Compared with RG and previously reported recycled graphite materials, ARG in our work activates the Li^+ storage capacity as well as accelerates Li^+ interfacial and bulk diffusion kinetics, thus achieving the outstanding capacity and rate performance (**Fig. 2f**, **Table S2**). Furthermore, the practical applicability of ARG was evaluated in a $LiFePO_4$||ARG cell configuration with the N/P ratio of 1.13. The assembled full cell delivers an initial discharge capacity of 116.08 mAh g^{-1} at 1C and retains 87.07% after 100 cycles, demonstrating the favorable cycling durability and promising potential of ARG for integration into practical commercial LIBs (**Fig. 2g**). As a result, the amorphous Al_2O_3 coating enables ARG with improved structural stability, additional Li^+ adsorption sites and regulated interfacial dynamics for high-performance and sustainable LIBs, particularly under high current conditions.

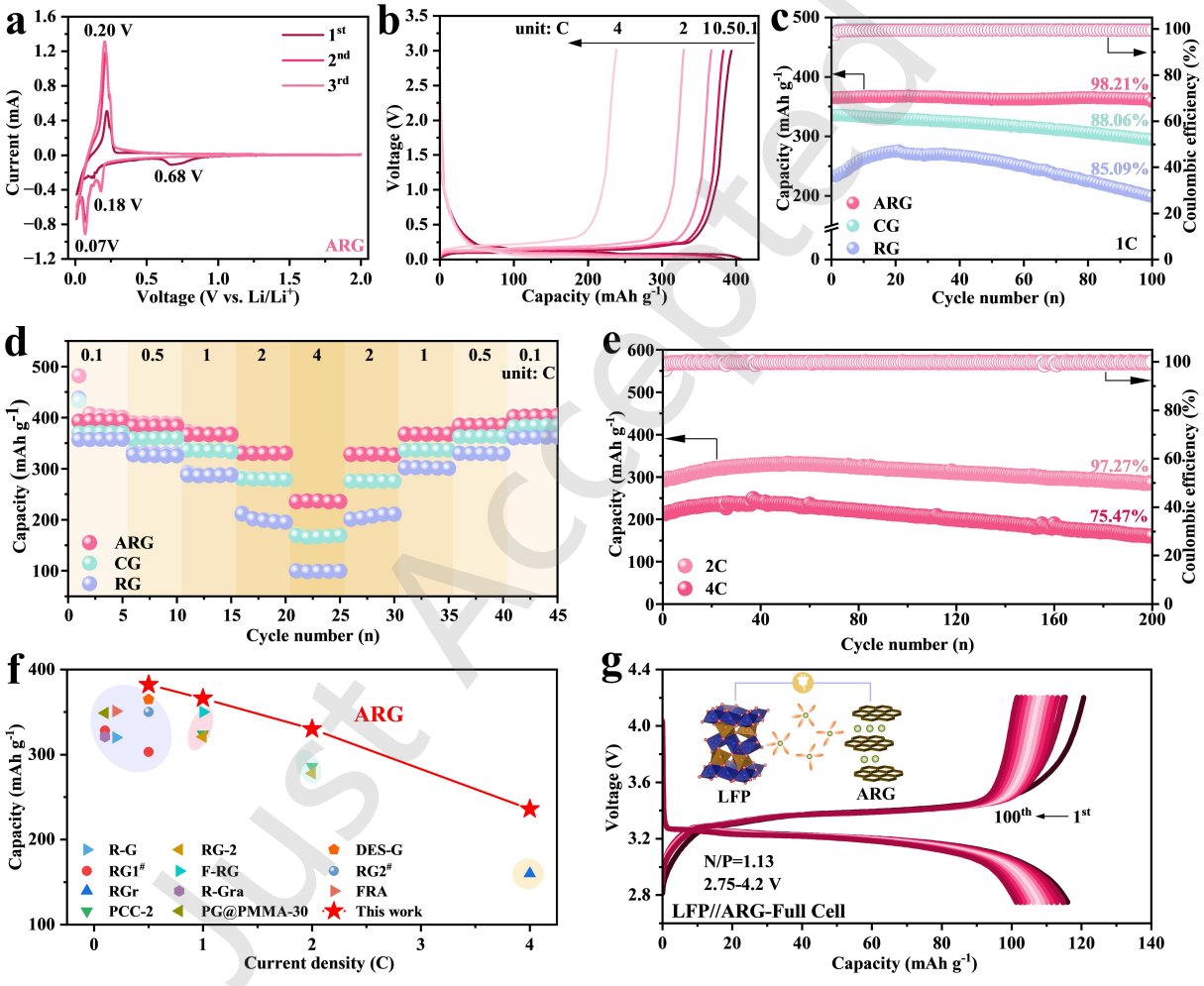


Fig. 2. Electrochemical performance of lithium batteries based on ARG, RG, and CG anodes. (a) CV profiles of the ARG electrode at 0.1 mV s^{-1}. (b) Voltage-capacity curves of ARG at different C rates. (c) The cycling performance of ARG, CG, and RG electrodes at 1C. (d) The rate performance of ARG, CG, and RG electrodes. (e) The cycling performance of ARG electrodes at 2C and 4C. (f) Comparison of the rate capability of ARG with recently reported regenerated graphite anodes. (g) Voltage-capacity curves of an assembled full cell (LFP||ARG) at 1 C.

To elucidate the mechanisms underlying the superior capacity and rate performance, the interfacial dynamics and structural evolution of ARG electrode were systematically investigated. Depending on the lithium storage mechanism, the total capacity of graphite can be divided into the "ramp capacity" and "plateau capacity" contributed by surface/marginal defect adsorption and Li^+ intercalation into graphite layers [33]. During the discharge process, the GCD curves of the three typical graphite electrodes exhibit a characteristic high-potential ramp followed by three distinct voltage plateaus at 0.1C (**Fig. 3a**). Specifically, the discharge plateaus of III, II, and I correspond to the sequential interlayer phase transitions of LiC_{18}, LiC_{12}, and LiC_6, respectively, induced by Li^+ embedding into graphite. Compared with RG and CG, the repaired ARG shows a significantly optimized capacity distribution, resulting from the effective interfacial regulation of the amorphous Al_2O_3 coating. In particular,

Just Accepted

ARG not only significantly reduces the proportion of slope capacity caused by serious structural damage of cracks and defects in RG, but also has a higher platform capacity ratio than RG and CG, especially in stage I of deep lithium intercalation (**Figs. 3b**, **S13**). This demonstrates that ARG can effectively repair damaged lattices through a targeted interface remodeling mechanism, thereby constructing multidimensional ion diffusion channels for accelerated lithium-ion insertion kinetics. The pore size distribution curves show that ARG contains more mesopores/macropores in the 10-100 nm range than RG and CG (**Fig. 3c**). Such a highly porous interface of Al_2O_3 layer with a large specific surface area endows ARG electrode with abundant physical Li^+ adsorption sites and efficient ion-permeation channels for high capacity and superior rate performance of ARG||Li cell (**Fig. S14**). To further evaluate the enhanced reaction kinetics improved by Al_2O_3 interface, CV curves of ARG and CG electrodes were recorded at different scan rates (**Figs. 3d**, **S15**). Compared with CG, ARG exhibits better shape retention and more symmetrical redox peaks along with the increased scanning rates, indicating its significantly enhanced charge diffusion kinetics for fast-charging ARG [34]. In contrast, the redox peak position significantly shifted, and the peak current exhibited an abnormal decrease in RG when the scanning speeds over 0.6 mV s^{-1}, re-confirming rapid Li^+ storage ability of ARG with high-efficient interfacial regulation (**Fig. S16**).

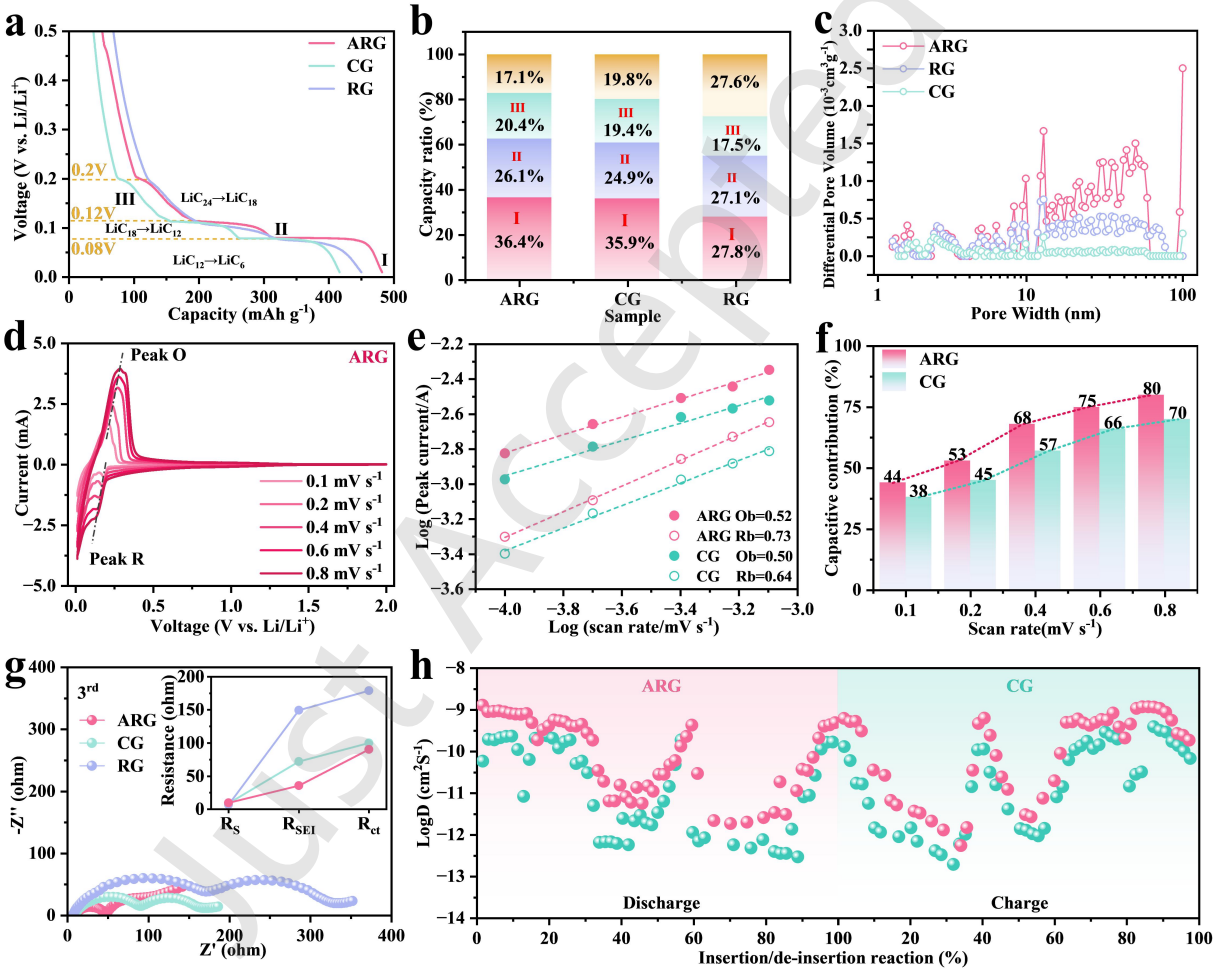


Fig. 3. Kinetic analysis of redox reaction in ARG, RG, and CG. (a) Initial discharge curves, and (b) capacity contribution ratios at different stages in the initial discharge process of ARG, CG, and RG at 0.1C. (c) Pore size distribution of ARG, CG, and RG. (d) CV curves of ARG at different scan rates. (e) b-value plots of ARG and CG. (f) Capacitive contributions of ARG and CG. (g) EIS curves of the three electrodes after 3rd cycle. (h) Corresponding ion diffusion coefficients of ARG and CG at different working states.

Furthermore, ARG electrode exhibits calculated b values of 0.52 and 0.73 for oxidation (O) and reduction (R) peaks, respectively, which are higher than those of RG (0.50, 0.64, respectively), as shown in **Fig. 3e** [35]. This demonstrates that Li^+ diffusion kinetics are significantly accelerated and that Li deposition on the graphite surface is effectively suppressed, reflecting the effectiveness of the alumina layer with abundant surface/edge active sites and Li^+ transport channels for fast-charging applications. Moreover, the capacitive contribution ratios of ARG range from 44% to 80% along with the scanning rate from 0.4 to 0.8 mV s^{-1}, significantly higher than those of CG (38% to 70%), indicating the rapid charge transfer dynamics regulated by multifunctional Al_2O_3 interface (**Fig. 3f**) [36]. Further details of the capacitive contribution curves of the two typical electrodes are shown in **Figs. S17** and **S18**.

Just Accepted

Based on the Nyquist plots, an appropriate equivalent circuit model was used to analyze the ohmic resistance (R_s), SEI impedance (R_{SEI}), and charge transfer impedance (R_{ct}) obtained from electrochemical impedance spectroscopy (EIS) data of ARG, CG, and RG at the initial 3rd cycle (**Fig. S19**). Besides the smallest R_s, ARG exhibits the lowest R_{SEI} (35.63 Ω) and R_{ct} (90.12 Ω) compared to those of CG (72.23 Ω, 99.94 Ω) and RG (149.42 Ω, 178.92Ω), suggesting a highly ion-conductive SEI film as well as fast interfacial charge transfer kinetics of ARG (**Fig. 3g**, **Table S3**). Galvanostatic intermittent titration technique (GITT) measurements reveal that the Li^+ diffusion coefficient (D_{Li^+}) of ARG is significantly higher than that of CG and RG, especially in the phase transition plateau region, indicating favorable interactions between Lewis-acidic Al sites and electrolytic anions that reduce migration resistance and enhance Li^+ adsorption (**Figs. 3h**, **S20, and S21**) [37]. Overall, the synergistic effect of amorphous alumina coating and lattice reconstitution of restored graphite endows ARG with rapid surface charge transfer and Li^+ bulk diffusion kinetics, enabling high-rate, stable, and sustainable LIBs.

To further explore the intrinsic fast-charging mechanism of ARG, the chemical composition of the electrode-electrolyte interface during cycling was systematically characterized by time-of-flight secondary ion mass spectrometry (TOF-SIMS) and XPS. For RG electrode, the TOF-SIMS analysis reveals that the SEI-related signals (LiF_2^-, $C_2H_2O^-$) exhibit a severe plaque-like heterogeneous distribution, originating from the local uneven electrolyte decomposition induced by surface defects and cracks on regenerated RG, as evidenced by the scattered high-intensity C_6^- signals (**Fig. 4a**). In sharp contrast, the ARG electrode demonstrates a highly uniform and continuous SEI layer with well-distributed LiF_2^- and $C_2H_2O^-$ species. Notably, the persistent and homogeneous Al^{3+} signal on the ARG surface confirms that the alumina coating maintains its structural integrity throughout cycling, effectively regulating interfacial reactions and forming a stable SEI comparable to that of CG (**Fig. S22**). Quantitative analysis of TOF-SIMS depth profiles reveals a clear compositional gradient within the interfacial layer tuned by alumina coating. As the sputtering depth increases, the content of inorganic components in the SEI layer first increases and then decreases, while the content of outer-layer organic components gradually diminishes (**Fig. 4b**) [38]. Besides the thinner overall thickness, the SEI layer formed on the ARG electrode contains significantly more LiF and less $C_2H_2O^-$ than that on RG. This is because the alumina coating suppresses excessive electrolyte decomposition, enabling the formation of a dense, LiF-rich interphase (**Fig. 4c**). Moreover, XPS analysis of the three typical graphite electrodes further confirms the optimized SEI composition regulated by the uniform Al_2O_3 interphase. Compared with CG and RG, the ARG electrode exhibits the highest LiF peak intensity, indicating that alumina modification promotes the formation of a LiF-rich SEI layer and suppresses the decomposition of fluorinated organic substances (**Fig. 4i, Fig. S23**) [39]. Different from RG, ARG exhibits a prominent $Li_xPO_yF_z$ peak and a negligible Li_3PO_4 signal, comparable to those of CG, suggesting well-constructed Li^+-conducting pathways rather than excessive electrolyte decomposition (**Fig. 4j, Fig. S22**) [40, 41]. Compared with RG, ARG exhibits markedly reduced intensities of organic species (C-O, C=O) and inorganic byproducts (Li_2CO_3) in C 1*s* and O 1*s* spectra, respectively, which is highly consistent with CG, confirming the suppressed electrolyte decomposition and the formation of a stable and dense SEI layer (**Fig. S24**).

Moreover, the ARG electrode exhibits a compact and crack-free surface morphology, with a moderate cross-sectional thickness expansion of only ~6.26 μm, obviously smaller than that of RG (~7.97 μm) after 300 cycles at 1C, indicating that alumina coating effectively buffers volume variation and maintains structural integrity of regenerated graphite after long-term cycling (**Fig. S25**). Combined with XPS and TOF-SIMS results, these findings confirm that the alumina interphase effectively suppresses uncontrolled electrolyte decomposition and promotes the formation of a dense, LiF-rich SEI layer, improving the interfacial stability and electrochemical performance of ARG. The aforementioned structural and compositional differences in the SEI layer are directly reflected in the reaction kinetics characterized by *in-situ* EIS tests of the three graphite electrodes during discharging and charging processes (**Figs. 4d–f**). Compared with RG and CG electrodes, ARG exhibits the lowest R_{SEI} and R_{ct} throughout cycling, indicating the fast and efficient interfacial charge transfer attributed to the alumina-induced, LiF-rich compact SEI layer with facilitated Li^+ diffusion kinetics (**Figs. 4g**, **h**) [42]. Although CG electrode has a relatively uniform interface, its impedance evolution indicates limited ion flux during the deep lithiation process, highlighting the critical role of the Al_2O_3 layer in overcoming the inherent kinetic bottleneck of conventional graphite. Based on the above electrode-electrolyte interface characterizations and *in-situ* kinetic analysis, the interfacial regulation mechanism of the ARG electrode is proposed (**Fig. 4k**). The abundant Lewis-acidic sites within the alumina layer interact favorably with electrolyte components to optimize the electrolyte decomposition pathway, thus promoting the formation of a spatially uniform and LiF-rich SEI layer on ARG surface even after long-term cycling. Meanwhile, the discontinuous alumina network utilizes the intrinsic defects in RG as preferential nucleation sites to construct rapid three-dimensional Li^+ transport pathways. These synergistic effects of alumina coating ensure efficient interfacial charge transfer and accelerated Li^+ diffusion kinetics, enabling fast-charging, stable ARG electrode.

Accepted

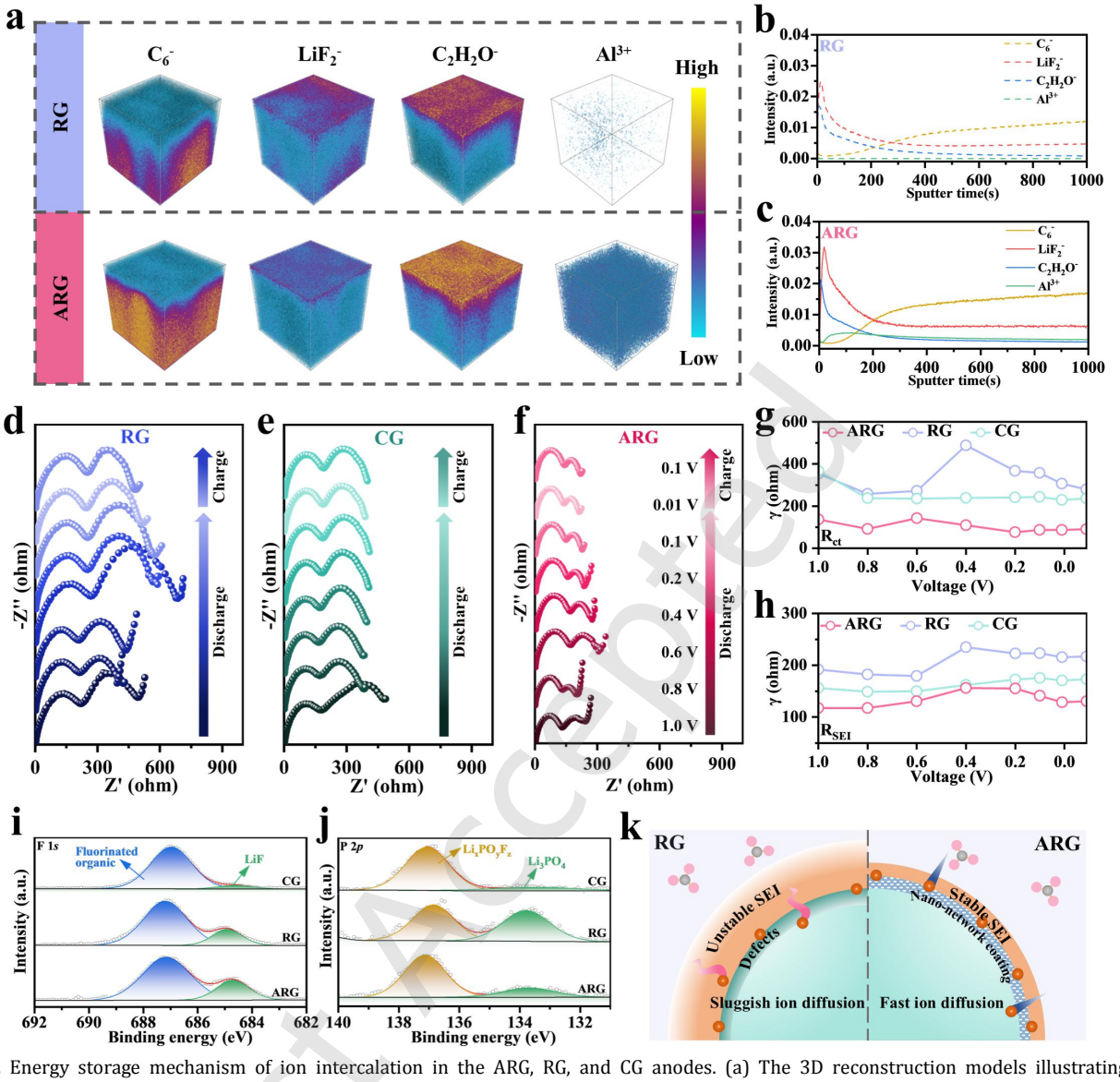


Fig. 4. Energy storage mechanism of ion intercalation in the ARG, RG, and CG anodes. (a) The 3D reconstruction models illustrating the distribution of C_6^-, LiF_2^-, $C_2H_2O^-$, and Al^{3+} on RG and ARG. The depth profiles obtained from TOF-SIMS of the SEI layer formed on (b) RG and (c) ARG. The in-situ EIS profiles of (d) RG, (e) CG, and (f) ARG. (g) R_{SEI} and (h) R_{ct} of ARG, RG, and CG. The XPS (i) F 1*s* and (j) P 2*p* spectra of CG, RG, and ARG anodes after 300 cycles at 1 C. (k) Schematic illustration of ion transportation.

To elucidate the interfacial kinetic advantages of the ARG electrode, density functional theory (DFT) was used to evaluate the Li^+ desolvation behavior and adsorption energy on defect-containing RG surfaces with/without Al_2O_3 modification. Given the high dielectric constant and strong coordination ability of ethylene carbonate (EC) solvent, $[Li(EC)_4]^+$ was selected as the initial solvation model [43, 44]. Notably, the energy changes during the gradual removal of the coordinating EC molecules reveal significantly different Li^+ desolvation behaviors on the surfaces of RG and ARG (**Fig. 5a**). Specifically, complete Li^+ desolvation on the ARG surface requires overcoming a cumulative energy barrier of 2.44 eV, significantly lower than the 4.31 eV on the RG surface. This enhanced Li^+ desolvation ability can be attributed to the weakened interactions between Li^+ and solvent molecules, enabled by Lewis-acidic Al^{3+} sites of Al_2O_3 coating that polarize Li^+–solvent coordination structures [45]. Besides, the polarized graphite/electrolyte interface can induce the decomposition of PF_6^-, driving the conversion of SEI components toward an inorganic LiF-rich phase for stable and highly ion-conductive transport pathways, which is consistent with the above TOF-SIMS and XPS results [46]. Furthermore, ARG exhibits stronger Li^+-trapping capability, with a much more negative Li^+ adsorption energy (−4.291 eV) than that of RG (−1.996 eV), which is attributed to the local electrostatic field environment jointly formed by bulk defects and Lewis-acidic Al^{3+} sites (**Fig. 5b**).

Overall, the porous Al_2O_3 nanonetwork provides continuous interfacial ion transport pathways distributed across the entire surface of graphite particles. Meanwhile, it further couples with intrinsic graphite defects at the interface, where defect sites act as preferential "entry

Just Accepted

points" for Li^+ to rapidly intercalate into the bulk, thus connecting interfacial percolation channels with intragranular defect diffusion paths to form a three-dimensionally interconnected ion transport network. Furthermore, the ARG with a uniform Al_2O_3 interphase realizes a desolvation-adsorption coupled transmission mechanism through the synergistic effect of defect-rich graphite and Lewis-acidic Al sites, which lowers Li^+ desolvation energy barriers and offers more adsorption sites to capture and stabilize desolvated Li^+, thereby substantially accelerating interfacial and bulk charge transfer kinetics and enhancing Li^+ storage ability for fast-charging and high capacity ARG.

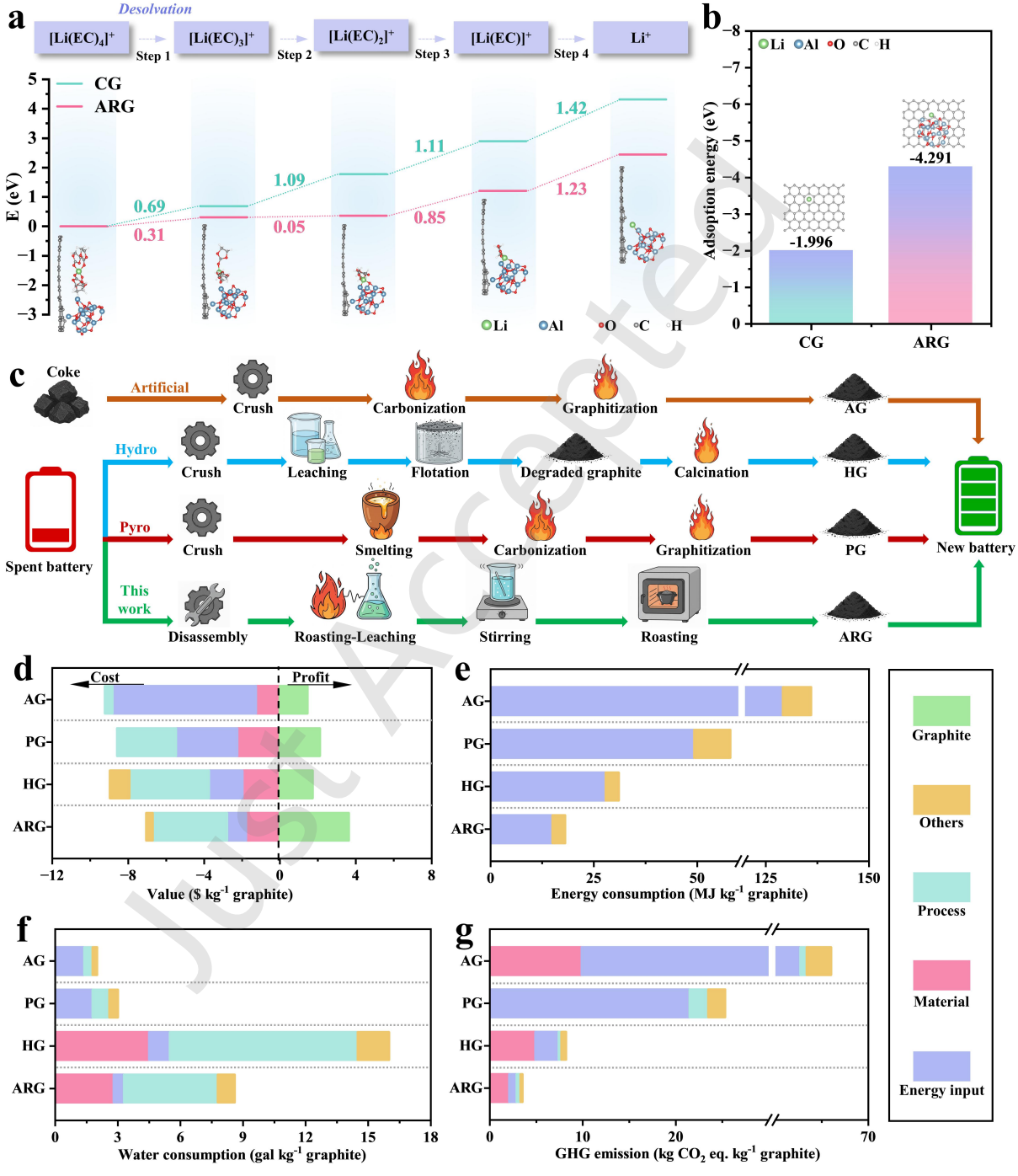


Fig. 5. Evidence for the superior electrochemical kinetics and integrated economic-environmental analyses of ARG. (a) The calculated desolvation energy changes of $[Li(EC)_4]^+$. (b) The calculated Li^+ adsorption energy of CG and ARG. (c) Schematic illustration of LIBs manufacturing using AG, HG, PG, and ARG . Comparison of different technologies for manufacturing 1 kg graphite in terms of (d) Cost and profit, (e) total energy consumption, (f) water consumption, and (g) greenhouse gas (GHG) emissions.

To objectively evaluate the economic and environmental sustainability of the ARG upcycling strategy, a comparative analysis was conducted on four typical graphite production/recycling routes, including artificial graphite

Just Accepted

(AG), pyrometallurgy (PG), hydrometallurgy (HG), and our proposed ARG process, using the GREET 2020 model developed by Argonne National Laboratory and relevant references (**Fig. 5c**) [47-49]. The ARG recovery process combines liquid-phase-assisted coating and low-temperature *in-situ* oxidation for targeted bulk modification and interfacial reconstruction, which avoids high-energy-consuming steps (such as graphitization and flotation), and demonstrates the best economic performance. Specifically, the production cost of ARG recovery process is only \$7.05 kg^{-1}, significantly lower than those of PG (\$8.58 kg^{-1}), HG (\$8.96 kg^{-1}), and AG synthesis (\$9.23 kg^{-1}). Furthermore, the potential profitability of recovered ARG is ~ \$3.63 kg^{-1}, much higher than that of PG (\$2.11 kg^{-1}), HG (\$1.72 kg^{-1}), and AG synthesis (\$1.45 kg^{-1}), all evaluated based on the costs and market prices of battery-grade graphite (**Fig. 5d**). From an environmental perspective, the ARG process also exhibits substantial advantages in terms of energy consumption, carbon emissions and water usage over the other three conventional routes. **Fig. 5e** reveals that the total energy consumption of the ARG process is only 18 MJ kg^{-1}, significantly lower than that of HG synthesis (31 MJ kg^{-1}), PG synthesis (58 MJ kg^{-1}) and AG synthesis (136 MJ kg^{-1}), reflecting the superior energy efficiency of the ARG upcycling method. Although the ARG process requires the use of ethanol and NMP as treatment media, leading to a moderate increase in water consumption (8.6 gal $kg_{graphite}^{-1}$) compared with AG and PG, its overall water usage is still substantially lower than that of conventional HG (16 gal $kg_{graphite}^{-1}$), as shown in **Fig. 5f**. Most critically, the ARG strategy yields the lowest greenhouse gas emissions with a mere 3.5 kg CO_2 eq. kg^{-1} among the four typical graphite production/recycling technologies, especially in comparison to the AG production process (66 kg CO_2 eq. kg^{-1}), demonstrating the minimal carbon footprint of ARG (**Fig. 5g**). More details of the economic and environmental analyses can be found in **Tables S4-S7**. Collectively, these results confirm that the ARG recycling process not only delivers exceptional economic benefits but also exhibits outstanding environmental compatibility, representing a highly sustainable and industrially viable approach for transforming spent graphite into fast-charging and durable graphite electrodes for advanced LIBs.

3 Conclusions

In summary, we present a catalytic–percolative interfacial engineering strategy to upgrade spent graphite from structural restoration toward targeted functional reconfiguration. By constructing an amorphous Al_2O_3 nanonetwork onto defect-rich graphite surface, a coupled graphite/Al_2O_3 interphase with bulk defects and Lewis-acidic Al^{3+} sites is established to cooperatively regulate the local electrochemical environment of the ARG electrode. Various *in*/*ex-situ* analyses combined with theoretical calculations reveal that such a catalytic-percolative interface markedly lowers the Li^+ desolvation energy barrier and strengthens interfacial Li^+ adsorption, thereby facilitating charge transfer across the electrode/electrolyte interface and enhancing lithium-ion storage capability. Meanwhile, the porous Al_2O_3 nanonetwork integrates with intrinsic graphite defects to form multidimensional ion transport pathways and promotes the formation of a stable, LiF-rich inorganic SEI layer, effectively suppressing parasitic reactions and reducing interfacial resistance. As a result, the ARG anode delivers an ultra-high reversible capacity, superior rate capability, and long-term cycling stability even under fast-charging conditions. Beyond excellent electrochemical performance, the proposed ARG upcycling route exhibits distinct advantages in terms of economic and environmental sustainability. Therefore, this study unveils a coupled desolvation–adsorption–transport mechanism via interfacial catalytic-percolative engineering, representing a highly sustainable and industrially viable approach for transforming spent graphite into fast-charging and durable graphite anodes for advanced lithium-ion batteries.

Acknowledgements

This work was supported by the National Natural Science Foundation of China (grant numbers 52374410), Beijing Natural Science Foundation (grant numbers Z220021), Beijing Outstanding Young Scientists Program (grant numbers BJJWZYJH01201910007023).

Declaration of conflicting interests

The authors declare no conflicting interests regarding the content of this article.

Data availability

All data needed to support the conclusions in the paper are presented in the manuscript and/or the Supplementary Materials. Additional data related to this paper may be requested from the corresponding author upon request.

Electronic Supplementary Material: Supplementary material (experimental section; materials characterizations; electrochemical characterizations, DFT calculations and cost analysis) is available in the online version of this article at https://doi.org/10.26599/NRE.2026.9120276.

References

[1] Ma, R.; Tao, S.; Sun, X.; Ren, Y.; Sun, C.; Ji, G.; Xu, J.; Wang, X.; Zhang, X.; Wu, Q.; Zhou, G. Pathway decisions for reuse and recycling of retired lithium-ion batteries considering economic and environmental functions. *Nat. Commun.* **2024**, *15,* 7641.

[2] Yang, T.; Luo, D.; Zhang, X.; Gao, S.; Gao, R.; Ma, Q.; Park, H. W.; Or, T.; Zhang, Y.; Chen, Z. Sustainable regeneration of spent cathodes for lithium-ion and post-lithium-ion batteries. *Nat. Sustain.* **2024**, *7,* 776-785.

[3] Liu, W.; Peng, L.; Liu, M.; Peng, J.; Zeng, Z.; Cheng, S.; Xie, J.

In Press

Versatile chemical repair strategy for direct regeneration of cathode materials from retired lithium-ion battery. *Energy Storage Mater.* **2025**, *78,* 104227.

[4] Machala, M. L.; Chen, X.; Bunke, S. P.; Forbes, G.; Yegizbay, A.; de Chalendar, J. A.; Azevedo, I. L.; Benson, S.; Tarpeh, W. A. Life cycle comparison of industrial-scale lithium-ion battery recycling and mining supply chains. *Nat. Commun.* **2025**, *16,* 988.

[5] Xiao, Z.; Zheng, F.; Wang, Z.; Sun, Y.; Li, Z.; Sun, D.; Liao, S.; Pan, T.; Ye, Q.; Xu, C.; Li, Y. Regulating hard carbon microstructures on graphite anode toward splendid lithium-ion storage performance below 0.5 V. *Energy Storage Mater.* **2026**, *84,* 104777.

[6] Bhattacharyya, S.; Roy, S.; Lin, X.; Campagnol, N.; Vlad, A.; Ajayan, P. M. Graphite: the new critical mineral. *Nat. Rev. Mater.* **2026**, *11,* 65-78.

[7] Mao, Z.; Chai, J.; Wang, R. Toward sustainable lithium-ion batteries: Recycling and reuse strategies for spent graphite anodes. *Small* **2026**, *22,* e09952.

[8] Li, X.; Deng, C.; Liu, M.; Xiong, J.; Zhang, X.; Yan, Q.; Lin, J.; Chen, C.; Wu, F.; Zhao, Y.; Chen, R.; Li, L. Reutilization and upcycling of spent graphite for sustainable lithium-ion batteries: Progress and perspectives. *eScience* **2025**, *5,* 100394.

[9] Zhang, K.; Hu, Y.; Tang, S.; Hu, W.; Lin, J.; Zhang, H.; Peng, Y.; Tao, Y.; Liao, Y.; Lin, Y.; Pan, L.; Ding, M.; Liang, J.; Wei, Y.; Yang, L.; Chen, J.; Gong, Z.; Jin, Y.; Yang, Y. Decoupling electrolyte degradation pathways with diverse Li plating processes on graphite electrodes. *Adv. Energy Mater.* **2026**, e05230.

[10] Luo, S.; Liu, F. R.; Liu, Y.; Xu, Y. F.; Li, T.; Li, Z.; Chu, P. K.; Gao, B.; Zhou, G. M.; Huo, K. F. Direct construction of a LiF-rich interphase for sustainable regeneration of spent graphite electrodes via in situ decarbonization-fluorination strategy. *Adv. Mater.* **2025**, *38*, e14869.

[11] Da, H.; Pan, S.; Li, J.; Huang, J.; Yuan, X.; Dong, H.; Liu, J.; Zhang, H. Greatly recovered electrochemical performances of regenerated graphite anode enabled by an artificial PMMA solid electrolyte interphase layer. *Energy Storage Mater.* **2023**, *56,* 457-467.

[12] Hou, Y.; Guo, H.; Xing, B.; Zeng, H.; Kang, W.; Qu, X.; Zhang, C.; Jia, J.; Huang, G.; Cao, Y. Purification of spent graphite and surface modification with amorphous carbons as anodes for high-performance lithium-ion batteries. *Fuel* **2024**, *374,* 132488.

[13] Chen, W.; Qu, H. T.; Shi, R. Y.; Wang, J. X.; Ji, H. C.; Zhuang, Z. F.; Ma, J.; Tang, D.; Li, J. F.; Tang, J.; Ji, G. J.; Xiao, X.; Zhu, Y. F.; Zhou, G. M. Upcycling spent graphite into fast-charging anode materials through interface regulation. *ACS Energy Lett.* **2024**, *9,* 3505-3515.

[14] Da, H.; Fang, W.; Zhu, J.; Li, J.; Pan, S.; Li, J.; Huang, J.; Zhang, H.; Zhang, S. Superior rate capability of small regenerated graphite particles induced by homogeneously distributed current density derived from cracks and intrinsic defects. *Small* **2023**, *19,* 2304060.

[15] Yi, C.; Ge, P.; Wu, X.; Sun, W.; Yang, Y. Tailoring carbon chains for repairing graphite from spent lithium-ion battery toward closed-circuit recycling. *J. Energy Chem.* **2022**, *72,* 97-107.

[16] Liu, H.; Xu, Y.; Xiao, S.; Wang, W.; Huang, L.-B.; Jia, S.; Guo, Y.-J.; Zhang, Y.; Guo, Y.-G. Regulating the nanosheets structures in pitch-derived amorphous carbons for efficient sodium-ion storage. *Angew. Chem. Int. Ed.* **2025**, *64,* e202507996.

[17] Kawabata, K.; Yoshimatsu, H.; Fujii, E.; Hiragushi, K.; Osaka, A.; Miura, Y. Fluidity of a slurry of the graphite powder coated with Al_2O_3-based metal oxides. *J. Materi. Sci. Lett.* **2001**, *20,* 851-853.

[18] Rhee, D. Y.; Kim, J.; Moon, J.; Park, M.-S. Off-stoichiometric TiO_{2-x}-decorated graphite anode for high-power lithium-ion batteries. *J. Alloys Compd.* **2020**, *843,* 156042.

[19] Jin, P.; Zhang, X.; Li, L.; Ma, X.; Chong, Y.; Pruksawan, S.; Wang, F. Preparation of SnO_2@graphite anode based on the oriented deposition methodology with superior electrode behavior for Li ion battery. *ChemNanoMat*, **2024**, *10,* e202300509.

[20] Feng, T.; Xu, Y.; Zhang, Z.; Du, X.; Sun, X.; Xiong, L.; Rodriguez, R.; Holze, R. Low-cost Al_2O_3 coating layer as a preformed SEI on natural graphite powder to improve coulombic efficiency and high-rate cycling stability of lithium-ion batteries. *ACS Appl. Mater. Interfaces* **2016**, *8,* 6512-6519.

[21] Ma, H.; Yu, Z.; Chen, J.; Wang, D.; Dong, C.; Mao, Z. Incorporating α-Al_2O_3 nanodots into expanded graphite anodes toward stable fast charging for lithium-ion batteries.*ACS Appl. Energy Mater.* **2023**, *6,* 1389-1395.

[22] Choi, J. H.; Lee, H. G.; Lee, M. H.; Lee, S. M.; Kang, J.; Suh, J. H.; Park, M. S.; Lee, J. W. Multi-interface strategy for electrode tailoring toward fast-charging lithium-ion batteries. *Adv. Funct. Mater.* **2024**, *34*, 2400414.

[23] He, Y.; Yu, X.; Wang, Y.; Li, H.; Huang, X. Alumina-coated patterned amorphous silicon as the anode for a lithium-ion battery with high coulombic efficiency. *Adv. Mater.* **2011**, *23,* 4938-4941.

[24] Jung, Y. S.; Cavanagh, A. S.; Riley, L. A.; Kang, S.-H.; Dillon, A. C.; Groner, M. D.; George, S. M.; Lee, S.-H. Ultrathin direct atomic layer deposition on composite electrodes for highly durable and safe Li-ion batteries. *Adv. Mater.* **2010**, *22,* 2172-2176.

[25] Illarionov, Y. Y.; Knobloch, T.; Jech, M.; Lanza, M.; Akinwande, D.; Vexler, M. I.; Mueller, T.; Lemme, M. C.; Fiori, G.; Schwierz, F.; Grasser, T. Insulators for 2D nanoelectronics: the gap to bridge. *Nat. Commun.* **2020**, *11,* 3385.

[26] Chen, J. X.; Chen, P. G.; Zhu, Y. L.; Chen, F.; Qiao, M. K.; Wu, J.; Li, X. C. Modulation of carbon atom hybridization structure and electromagnetic absorption properties in carbon fiber composites. *Carbon* **2025**, *245,* 10.

[27] Usman, M.; Arshad, M.; Suvanam, S. S.; Hallén, A. Influence of annealing environment on the ALD-Al_2O_3/4H-SiC interface studied through XPS. *J. Phys. D Appl. Phys.* **2018**, *51,* 105111.

[28] Kim, D. S.; Kim, Y. E.; Kim, H. Improved fast charging capability of graphite anodes via amorphous Al_2O_3 coating for high power lithium ion batteries. *J. Power Sources*, **2019**, *422,* 18-24.

[29] Zhang, T.; Shi, X.; Jin, J.; Wang, R.; Gong, Y.; Wang, S.; Wang, H. Laser-driven upcycling of spent graphite into interlayer-expanded carbon nanocages for fast and stable K^+/Li^+ storage. *Energy Storage Mater.*, **2026**, *84,* 104847.

[30] Yan, Q. Y.; Xu, L. Q. Y.; Zhao, Y.; Wu, F.; Chen, R. J.; Li, L. Regenerated graphite-derived cellular-inspired polydopamine@NiO@graphite toward robust lithium storage. *Appl. Mater. Interfaces* **2023**, *15,* 25506-25515.

[31] Yang, G.; Li, X.; Guan, Z.; Tong, Y.; Xu, B.; Wang, X.; Wang, Z.; Chen, L. Insights into lithium and sodium storage in porous carbon. *Nano Lett.* **2020**, *20,* 3836-3843.

[32] Zhu, H.; Shiraz, M. H. A.; Liu, L.; Hu, Y.; Liu, J. A facile and low-cost Al_2O_3 coating as an artificial solid electrolyte interphase layer on graphite/silicon composites for lithium-ion batteries. *Nanotechnology* **2021**, *32,* 144001.

[33] Liu, X.; Yin, L.; Ren, D.; Wang, L.; Ren, Y.; Xu, W.; Lapidus, S.; Wang, H.; He, X.; Chen, Z.; Xu, G.-L.; Ouyang, M.; Amine, K. In situ observation of thermal-driven degradation and safety concerns of lithiated graphite anode. *Nat. Commun.* **2021**, *12,* 4235.

[34] Aoki, K. J.; Chen, J.; Liu, Y.; Jia, B. Peak potential shift of fast cyclic voltammograms owing to capacitance of redox reactions. *J. Electroanal. Chem.* **2020**, *856,* 113609.

[35] Gong, S. E.; Sun, K. S.; Cao, N. Z.; Chao, D. M.; Jia, X. T.; Wang, C. Y. Potassium phthalimide doped with delta-site structures to construct ultra-long cycle life aqueous Zn-polymer batteries. *Adv. Funct. Mater.* **2024**, *34*, 2409805.

[36] Yang, Z.; Huang, X.; Meng, P.; Jiang, M.; Wang, Y.; Yao, Z.; Zhang, J.; Sun, B.; Fu, C. Phenoxazine polymer-based p-type positive

Just Accepted

electrode for aluminum-ion batteries with ultra-long cycle life. *Angew. Chem. Int. Ed.* **2023**, *62,* e202216797.

[37] Oyakhire, S. T.; Liao, S.-L.; Shuchi, S. B.; Kim, M. S.; Kim, S. C.; Yu, Z.; Vilá, R. A.; Rudnicki, P. E.; Cui, Y.; Bent, S. F. Proximity matters: Interfacial solvation dictates solid electrolyte interphase composition. *Nano Lett.* **2023**, *23,* 7524-7531.

[38] Liu, Y.; Shi, H.; Yang, M.; Wang, H.; Ma, Y.; Li, X.; Jin, D.; Ma, C.; Ren, Z.; Shi, X.; Zhou, F.; Wu, Z.-S. Kilogram-Scale Production of Ultrafast-charging micro-expanded graphite anode toward high-power and long-life Ah-level pouch batteries. *Adv. Mater.* **2025**, *37,* e06584.

[39] Liu, X.; Li, S.; Yuan, C.; Zheng, B.; Cheng, G.; Chen, Y.; Lu, X.; Gu, D.; Lv, B.; Li, H.; Yan, Z.; Qian, H.; Zhu, Y.; Sun, D.; Song, Y.; Xiang, Y. Probing the heterogeneous nature of LiF in solid–electrolyte interphases. *Nature* **2025**, *646,* 102-107.

[40] Guo, Y.; Pan, S.; Yi, X.; Chi, S.; Yin, X.; Geng, C.; Yin, Q.; Zhan, Q.; Zhao, Z.; Jin, F.-M.; Fang, H.; He, Y.-B.; Kang, F.; Wu, S.; Yang, Q.-H. Fluorinating all interfaces enables super-stable solid-state lithium batteries by in situ conversion of detrimental surface Li_2CO_3. *Adv. Mater.*, **2024**, *36,* 2308493.

[41] Pan, T.; Yang, P.; Zhang, S.; Guo, Q.; Zheng, C.; Liu, S.; Li, Y.; Sun, W. Adjacent element induction and weak solvation effects enable thermal robust and fast-charging graphite anode for lithium-ion batteries. *Adv. Funct. Mater.*, **2026**, *36,* e27980.

[42] Lazanas, A. C.; Prodromidis, M. I. Electrochemical impedance spectroscopy-A tutorial. *ACS Meas. Sci. Au* **2023**, *3,* 162-193.

[43] Hossain, M. A.; Wu, D.; Zhu, Q.; Liu, Q.; Yang, J.; Xu, J.; Liu, C.; Kang, S.; Yang, Z.; Son, S.-B.; Yoo, D.-J.; Zhang, Z. High Li^+ Transference number electrolyte enabled by fluoride acceptor for low-temperature Li-ion batteries. *ACS Energy Lett.* **2025**, *10,* 3629-3637.

[44] Chen, Y. H.; Ma, Z.; Wang, Y. Q.; Kumar, P.; Zhao, F.; Cai, T.; Cao, Z.; Cavallo, L.; Cheng, H. R.; Li, Q.; Ming, J. Trace ethylene carbonate-mediated low-concentration ether-based electrolytes for high-voltage lithium metal batteries. *Energy Environ. Sci.* **2024**, *17,* 5613-5626.

[45] Jiang, J.; Liu, J.; Zheng, X.; Li, L.; Huang, J.; Wang, Y.; Guo, S.; Zhang, Y.; Yang, X.; Wen, J.; Zhao, B.; Jiang, Y.; Sun, X.; Zhang, J.; Wu, C.; Dou, S. Tailoring a fast ion-conducting substrate with competitive adsorption for dendrite-free lithium/potassium metal batteries. *Angew. Chem. Int. Ed.* **2025**, *64,* e202510178.

[46] Li, F. C.; Li, Y.; Li, H. J.; Ren, L.; Hu, J. P.; Ma, C.; Zhu, A. N.; Wu, S.; Gu, X.; Wu, M. B. AlF3-stabilized cathode electrolyte interphase with superior PF_6^- affinity and PF_6^- -transferred characteristics for dual-ion batteries. *Energy Storage Mater.*, **2025**, *80,* 9.

[47] Luo, S.; Liu, F.; Tianxu, W.; Liu, Y.; Zhang, C.; Bie, C.; Liu, M.; Chu, P. K.; Huo, K.; Gao, B. Regeneration of spent graphite via graphite-like turbostratic carbon coating for advanced Li ion battery anode. *Energy Storage Mater.* **2024**, *73,* 103833.

[48] Ji, Y. S.; Zhang, H.; Yang, D.; Pan, Y. J.; Zhu, Z. L.; Qi, X. Q.; Pi, X. P.; Du, W. C.; Cheng, Z. H.; Yao, Y. G.; Qie, L.; Huang, Y. H. Regenerated graphite electrodes with reconstructed solid electrolyte interface and enclosed active lithium toward >100% initial coulombic efficiency. *Adv. Mater.* **2024**, *36*, 2312548.

[49] Rey, I.; Vallejo, C.; Santiago, G.; Iturrondobeitia, M.; Lizundia, E. Environmental impacts of graphite recycling from spent lithium-ion batteries based on life cycle assessment. *ACS Sustainable Chem. Eng.* **2021**, *9,* 14488-14501.

Under Accepted



Xueqian Li received M.S. degree from Beijing Institute of Technology in 2026. Now she is an engineer at Beijing Jingwei Hirain Technologies Co., Inc. Her current research interests include the recycling and regeneration of spent lithium-ion battery materials and their applications in energy·storage devices.



Xiaodong Zhang received the M.S. and Ph.D. degrees from Lanzhou University of Technology and Beijing Institute of Technology (BIT) in 2019 and 2025, respectively. Currently, he is a postdoctoral researcher at the School of Materials Science and Engineering, BIT. His research focuses on degradation mechanisms and resource recovery of lithium-ion batteries.



Yi Zhao received the B.S. degree from Yanshan University in 2014 and the Ph.D. degree from Beihang University in 2020. From 2020 to 2022, she conducted postdoctoral research at the School of Materials Science and Engineering, Beijing Institute of Technology (BIT). she is an associate professor at the College of Chemistry, Beijing University of Chemical Technology. Her research interest is mainly focused on key electrode materials and energy storage mechanism for energy storage batteries.



Li Li received her B.S. and Ph.D. degrees from the Shanxi University and Beijing Institute of Technology (BIT) in 1999 and 2004, respectively. Dr. Li is a currently a professor in Beijing Key Laboratory of Environmental Science and Engineering, School of Materials Science and Engineering, BIT, China. Her research interests focus on electrochemical energy storage and conversion technology and the recycling technique and life-cycle analysis for spent secondary batteries. As the principal investigator, Pro. Li successfully hosted the National Key Program for Basic Research of China, National High Tech 863 project, the National Natural Science Foundation, etc.

Just Accepted

Electronic Supplementary Material

Upcycling Spent Graphite into Fast-Charging and Sustainable Anodes via Interfacial Catalytic-Percolative Engineering

Xueqian Li [1,§], Xiaodong Zhang [1, §], Jiao Lin [1], Jiahui Lu [2], Yushuo Zhang [2], Qingrong Huang [1], Mengyao Liu [2], Meng Xu [2], Renjie Chen [1, 3, 4], Yi Zhao [2, 3] (✉), and Li Li [1, 3, 4] (✉)

[1] *Beijing Key Laboratory of Environmental Science and Engineering, School of Materials Science and Engineering, Beijing Institute of Technology, Beijing 100081, China*

[2] *State Key Laboratory of Chemical Engineering, College of Chemistry, Beijing University of Chemical Technology, Beijing 100029, China*

[3] *Shandong Key Laboratory of Advanced Chemical Energy Storage and Intelligent Safety, Advanced Technology Research Institute, Beijing Institute of Technology, Jinan 250300, China*

[4] *Innovative Research Team in High-Safety Energy Storage System and Smart Microgrids of Guangdong Province, Beijing Institute of Technology (Zhuhai), Zhuhai 519088, China*

[§] *Xueqian Li and Xiaodong Zhang contributed equally to this work.*

Supporting information to https://doi.org/10.26599/NRE.2026.9120276.

Just Accepted

Experimental Section

Recycling process of RG (recycling graphite): First, fully discharging the SLIBs, manually disassemble them to obtain the electrode sheets. Then, the obtained spent anode sheets are immersed in N-Methyl-pyrrolidone (NMP) solution to recover copper foil. Subsequently, the anode electrode powder was calcined in a muffle furnace to remove the binder and electrolyte. Finally, rinse with acid and deionized water to remove surface contaminants.

The preparation process of ARG electrode materials: Disperse the RG in anhydrous ethanol and stir at room temperature to form a uniform suspension. Slowly add aluminium nitrate nonahydrate ($Al(NO_3)_3{\cdot}9H_2O$, Macklin, ≥ 99.9%), and continuously stir to ensure thorough mixing. Under the stirring condition of 400 rpm, the mixed solution was heated to 65°C to allow the ethanol to completely evaporate, obtaining the precursor powder. The dried powder was transferred to a vertical furnace and heated to 600°C for 3h under air atmosphere with a heating rate of $5°C \cdot min^{-1}$, and finally Al_2O_3-coated regenerated graphite (ARG) was obtained. The final products were denoted as ARG-1, ARG-5, and ARG-10, corresponding to the mass ratios of RG to $Al(NO_3)_3{\cdot}9H_2O$ at 100:1, 20:1, and 10:1, respectively.

Material Characterization: The surface morphology and microstructure of the composite electrode materials were observed by scanning electron microscope (HitachiS-4800) and transmission electron microscope (FEI Talos F200X). Elemental mapping was obtained by using an energy-dispersive X-ray detector. The crystal structure of the samples was studied using the Rigaku Miniflex X-ray diffractometer. Raman spectra were obtained using a DXR Raman microscope with an excitation wavelength of 532 nm. The surface elements and chemical valence states of the samples were analyzed through X-ray photoelectron spectroscopy (XPS, Escalab 250 Xi, ThermoFisher Scientific) and time of flight secondary ion mass spectrometry (TOF-SIMS, M6, IONTOF GmbH). The specific surface area and pore size distribution of the samples were determined by Brunauer-Emmett-Teller (BET) analysis of nitrogen desorption-adsorption isotherms (ASAP2020, Micromeritics).

Electrochemical Measurements: Coin cells (CR2032) were assembled to test the electrochemical performance of ARG, RG, and CG. Mechanically mix graphite powders (80%), PVDF (10%), and carbon black (10%) in NMP solution to form a uniformly dispersed slurry. The slurry was coated on Cu foil and dried in an oven at 60°C for 6 h to obtain the anode plates with a 2 cm^{-2} active substance loading. The counter electrode used a Li metal disc with a diameter of 15 mm and a thickness of 0.45 mm. In addition, Celgard 2500 membranes and 1M $LiPF_6$ in EC:DMC:DEC (1:1:1 in volume) were used as the separator and electrolyte, respectively. Then, CR2025 coin cells were prepared in a glove box filled with argon (H_2O < 0.01 ppm, O_2 < 0.01 ppm). The assembly process of a full cell is similar to that of a half-cell, in which ARG was used as the anode material while cathode material was LFP. The cathode slurry is cast onto the Al foil, which is composed of LFP (80%), PVDF (10%), and carbon black (10%). And the negative-to-positive capacity ratio (N/P) was set to 1.1~1.2. To illustrate the influence of RGr on the formation of SEI, in situ EIS was conducted at 1.0, 0.8, 0.6, 0.4, 0.2, 0.1, and 0.01V during the first discharge and charge cycle. In addition, cyclic voltammetry (CV) measurements were carried out on the electrochemical workstation (CHI 604D), and electrochemical tests were performed on the Neware battery tester (CT-4008T).

Calculation Details: All density functional theory (DFT) calculations in this work were carried out using the Vienna Ab initio Simulation Package (VASP).[1, 2] The exchange–correlation potential were treated within the generalized gradient approximation (GGA) employing the Perdew–Burke–Ernzerhof (PBE) functional.[3] The interaction between valence

electrons and ionic cores was described by the projector augmented wave (PAW) method.[4] A plane-wave kinetic energy cutoff of 400 eV was applied for all calculations. Owing to the relatively large size of slabs, the Brillouin zone was sampled using a 2 × 2 × 1 K-point. The energy and force convergence criteria of the self-consistent iteration were set to 10^{-5} eV and 0.05 eV $Å^{-1}$, respectively. Long-range van der Waals (vdW) interactions were incorporated using the DFT-D3 correction scheme.[5] Structural models and calculation results were visualized with the VESTA software package.[6]

The adsorption energies (Eads) are calculated by:

$E_{ads} = E_{*Li} - E_{Li} - E_{sub}$

where E_{Li} and E_{*Li} represent the energies before and after the adsorption of Li on the substrate, respectively. E_{sub} is the energy of a clean surface.

The desolvation energies (△E) are calculated by:

$^{\triangle}E_1 = E[*Li\text{-}(EC)_3] + E(EC) - E[*Li\text{-}(EC)_4]$

$^{\triangle}E_2 = E[*Li\text{-}(EC)_2] + E(EC) - E[*Li\text{-}(EC)_3]$

$^{\triangle}E_3 = E[*Li\text{-}(EC)] + E(EC) - E[*Li\text{-}(EC)_2]$

$^{\triangle}E_4 = E[*Li] + E(EC) - E[*Li\text{-}(EC)]$

where $E[*Li\text{-}(EC)_n]$ (with n = 1, 2, 3, 4) and E_{*Li} represent the total energies of the system after the adsorption of Li-(EC) and a single Li on the substrate, respectively.

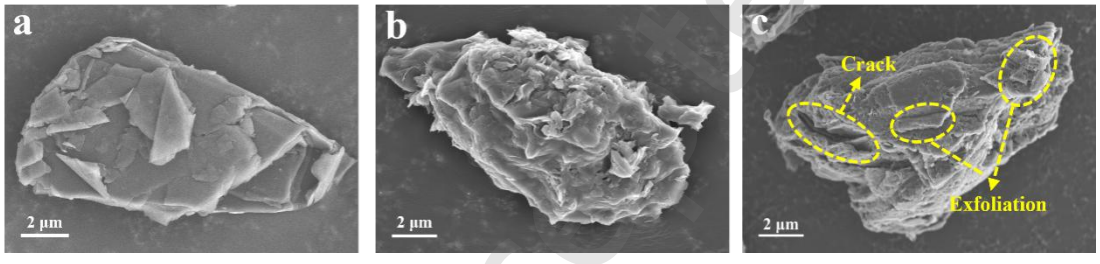


Fig. S1. The SEM images of CG (a), SG(b), and RG (c).

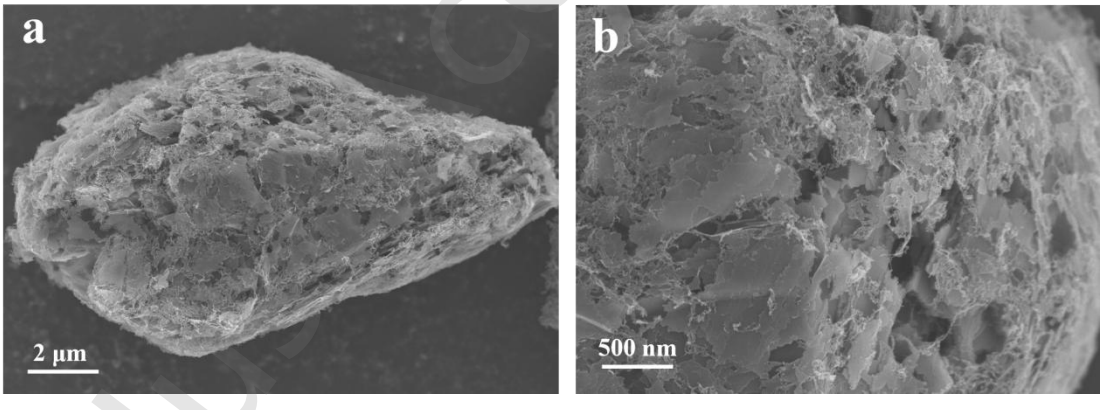


Fig. S2. The SEM images of ARG.

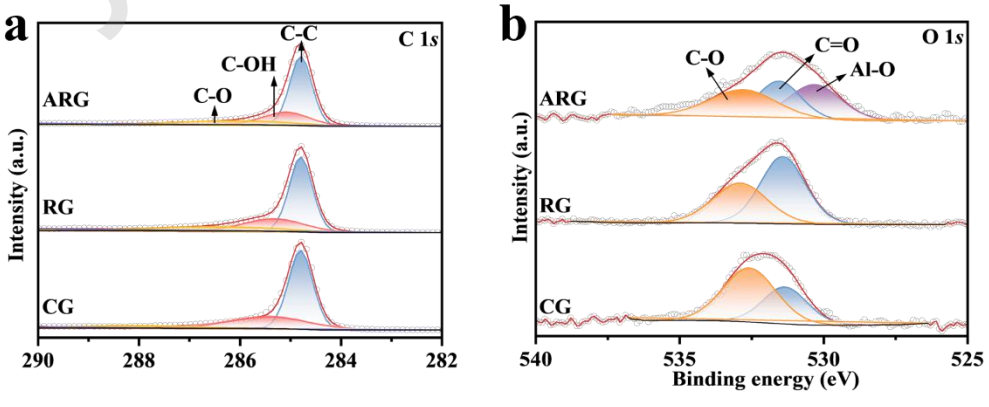


Fig. S3. XPS comparison of ARG, RG, and CG, (a) C 1*s* spectra and (b) O 1*s* spectra.

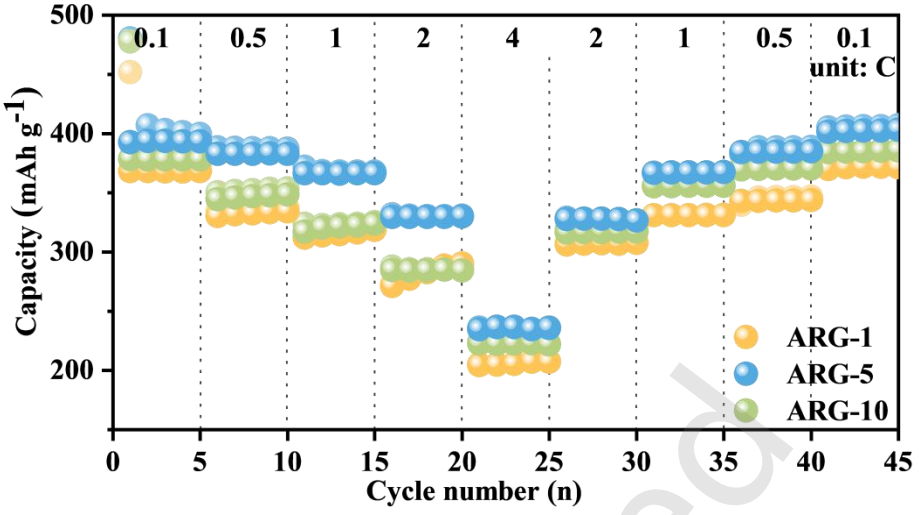


Fig. S4. The rate performance of ARG-1, ARG-5, and ARG-10 anodes with different Al_2O_3 doping ratios.

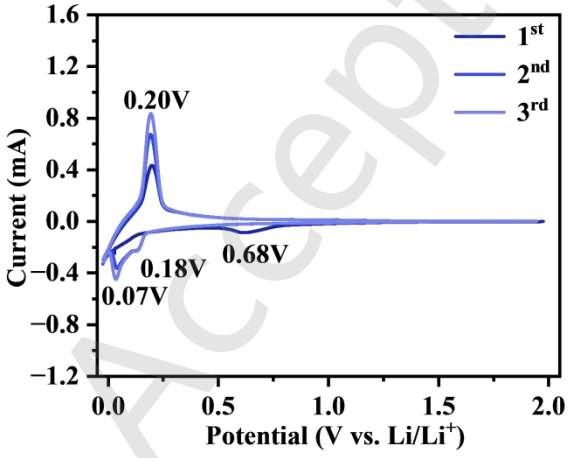


Fig. S5. CV profiles of the RG electrode at 0.1 mV s^{-1}.

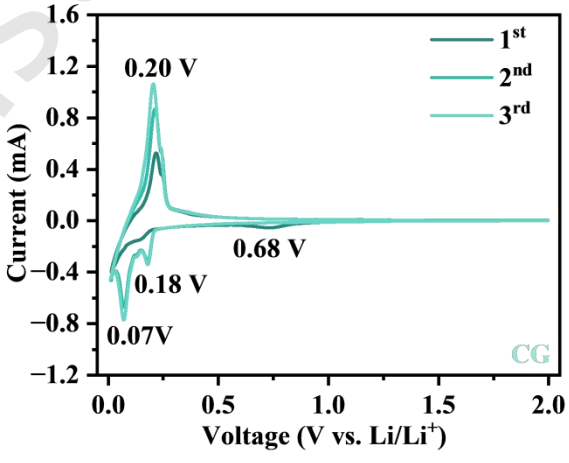


Fig. S6. CV profiles of the CG electrode at 0.1 mV s^{-1}.

Just Accepted

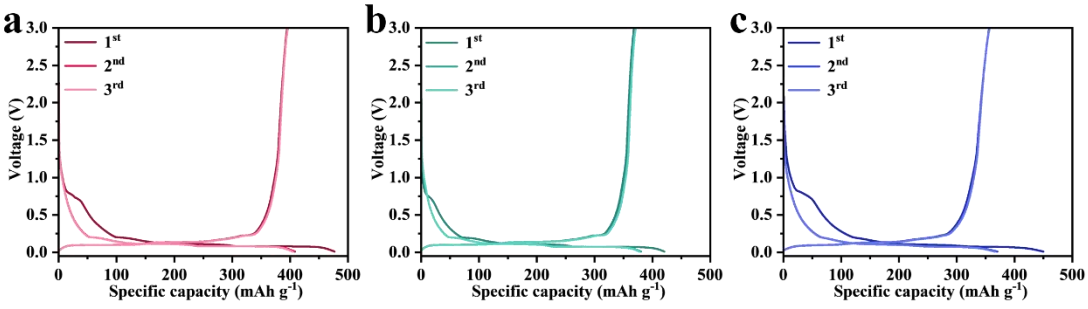


Fig. S7. The initial three cycles GCD curves of (a) ARG, (b) RG, and (c) CG at 0.1 C.

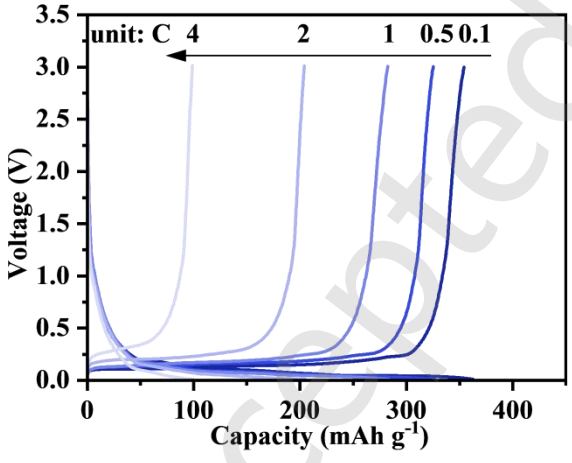


Fig. S8. Voltage-capacity curves of RG at different C rates (0.1, 0.5, 1, 2, and 4C).

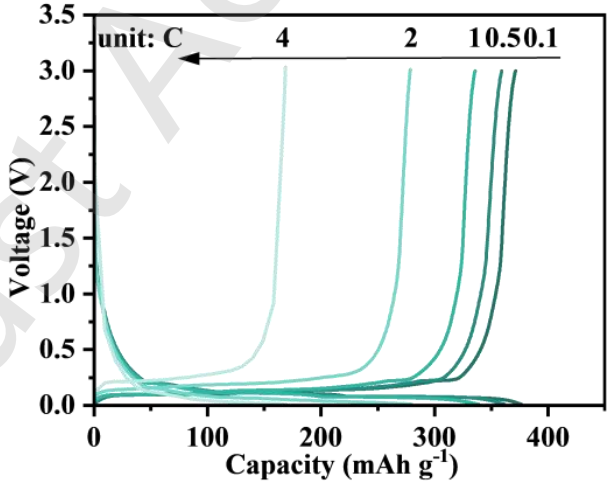


Fig. S9. Voltage-capacity curves of CG at different C rates (0.1, 0.5, 1, 2, and 4C).

Just Accepted

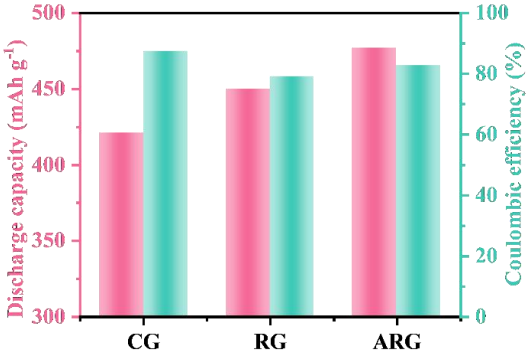


Fig. S10. Initial discharge capacity and initial coulombic efficiency of CG, RG, and ARG.

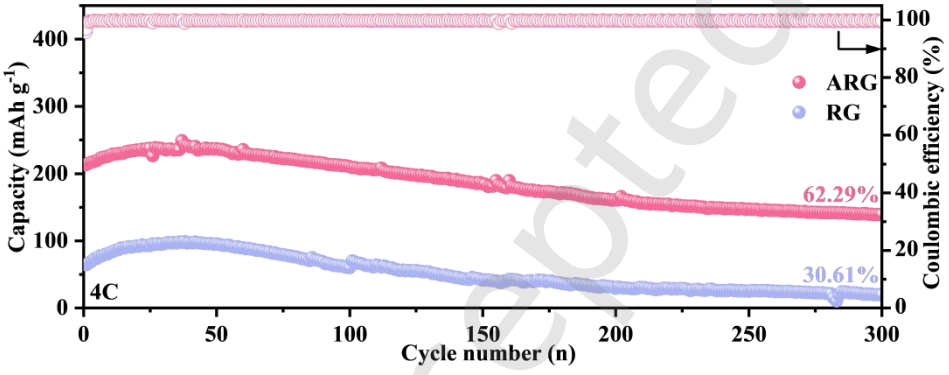


Fig. S11. The cycling performance of ARG and RG electrodes at 4C.

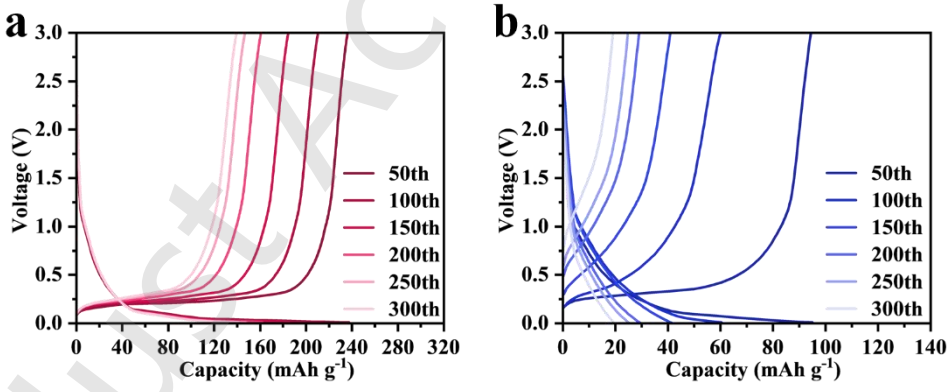


Fig. S12. The cycling performance of ARG and RG electrodes at 4C.

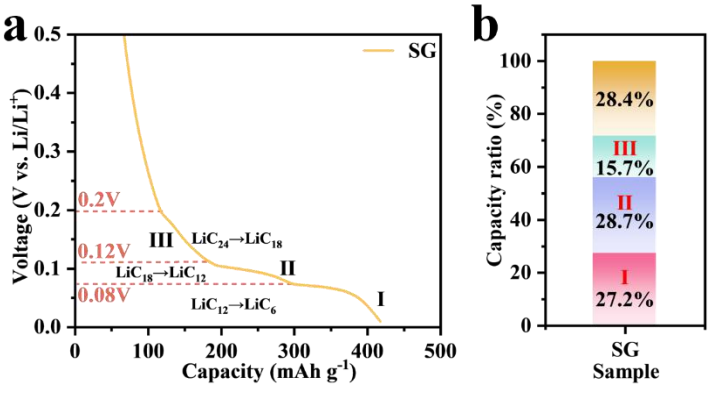


Fig. S13. (a) Initial discharge curves of SG at 0.1C. (b) Contribution rate of capacity at different stages in the initial discharge process.

Just Accepted

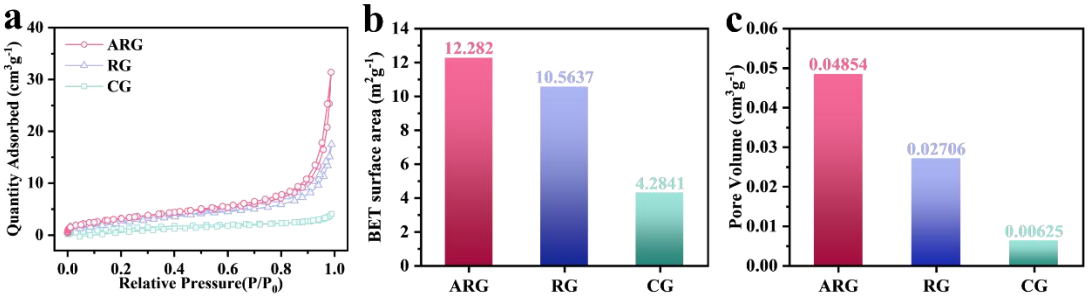


Fig. S14. (a) Nitrogen adsorption–desorption isotherms, (b) BET specific surface area, and (c) pore volume of ARG, RG, and CG.

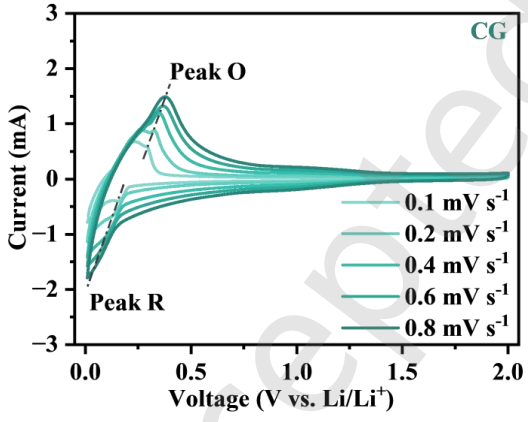


Fig. S15. CV curves of the CG with different scan rates.

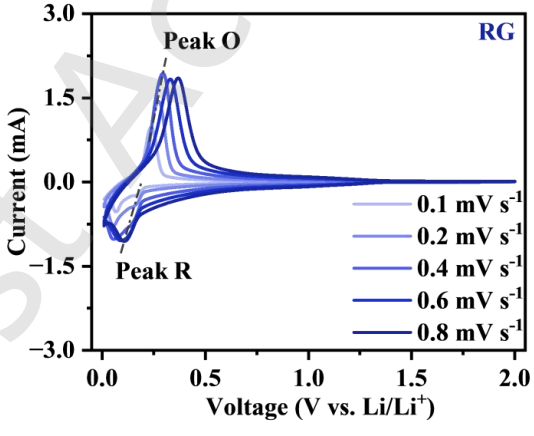


Fig. S16. CV curves of the RG with different scan rates.

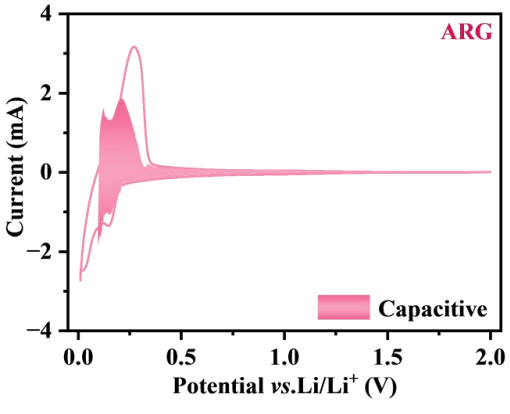


Fig. S17. Capacitive contribution curve of ARG at 0.4 mV s^{-1}.

Just Accepted

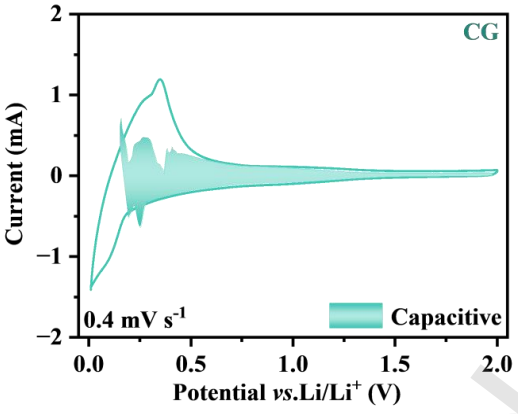


Fig. S18. Capacitive contribution curve of CG at 0.4 mV s^{-1}.

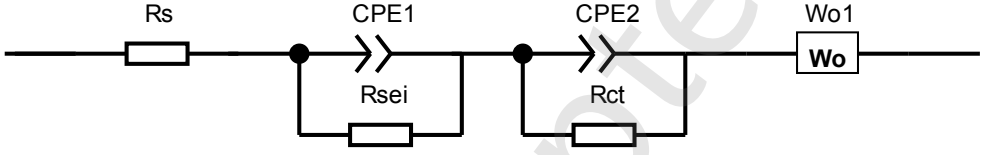


Fig. S19. The equivalent circuit of the ARG, RG and, CG electrode, where R_s, R_{sei}, R_{ct}, and Wo represent the internal resistance, SEI film interface resistance, charge transfer resistance and Warburg impedance, respectively.

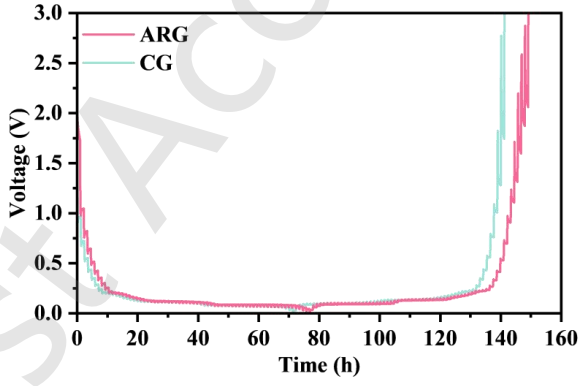


Fig. S20. Discharge-charge GITT curves for ARG and CG at 0.1 C.

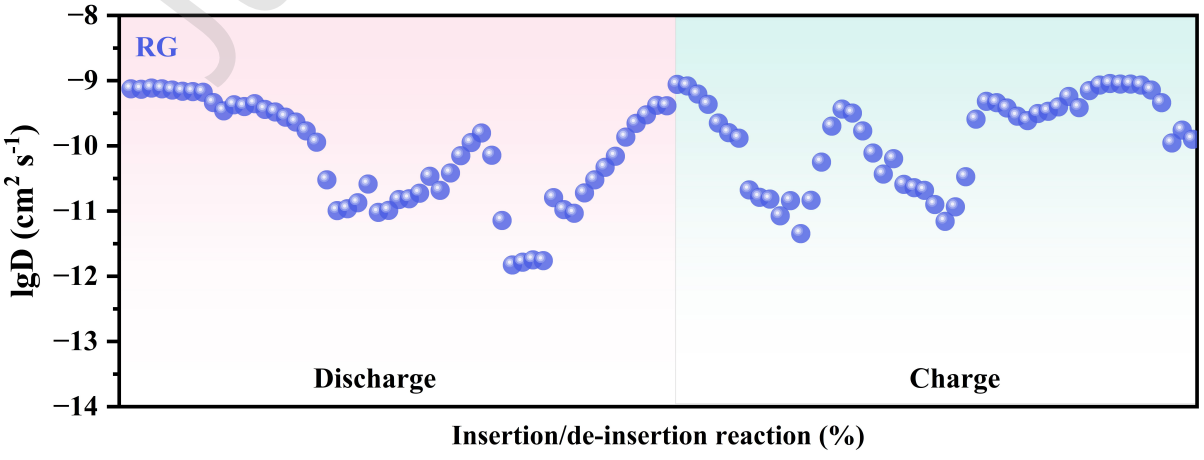


Fig. S21. Corresponding ion diffusion coefficients of RG at different working states.

Just Accepted

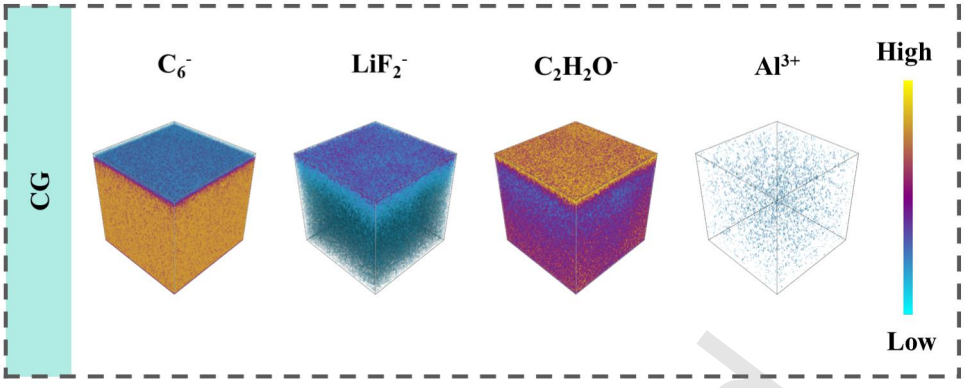


Fig. S22. 3D reconstruction models illustrating the distribution of C_6^-, LiF_2^-, $C_2H_2O^-$, and Al^{3+} on CG.

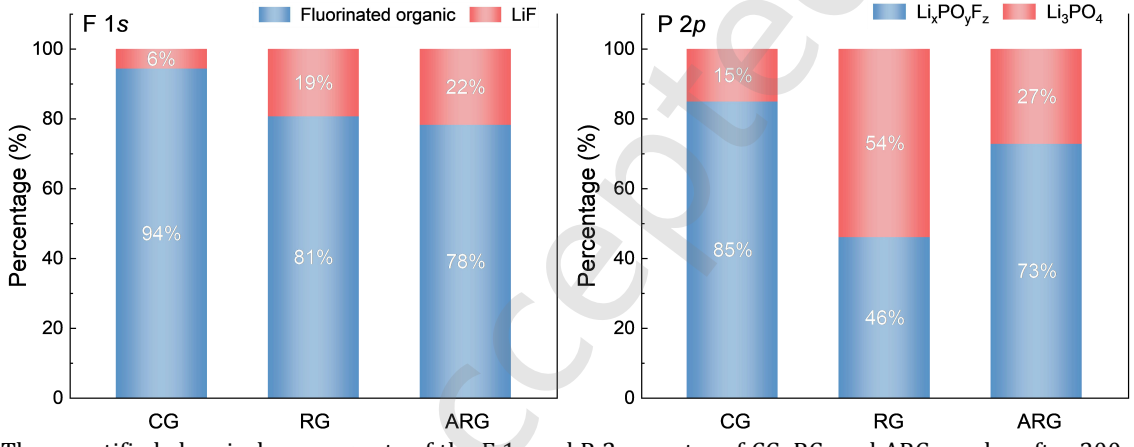


Fig. S23. The quantified chemical components of the F 1*s* and P 2*p* spectra of CG, RG, and ARG anodes after 300 cycles at 1C.

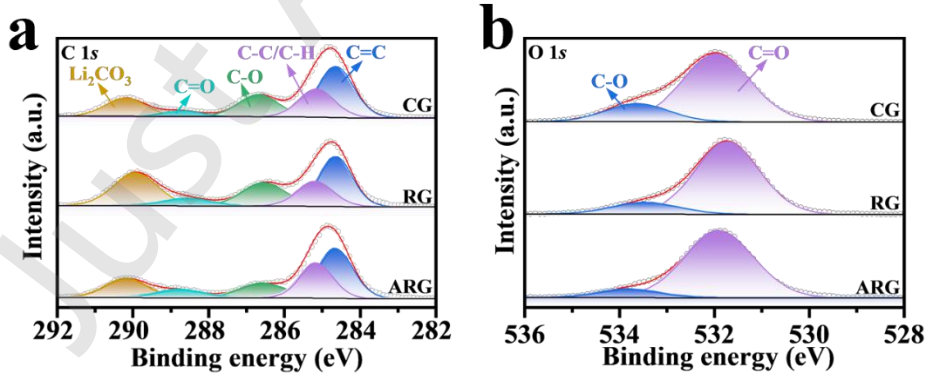


Fig. S24. SEI layers on the surface of CG, RG, and ARG anodes after 300 cycles at 1 C, (a) C 1*s*, (b) O 1*s*.

Just Accepted

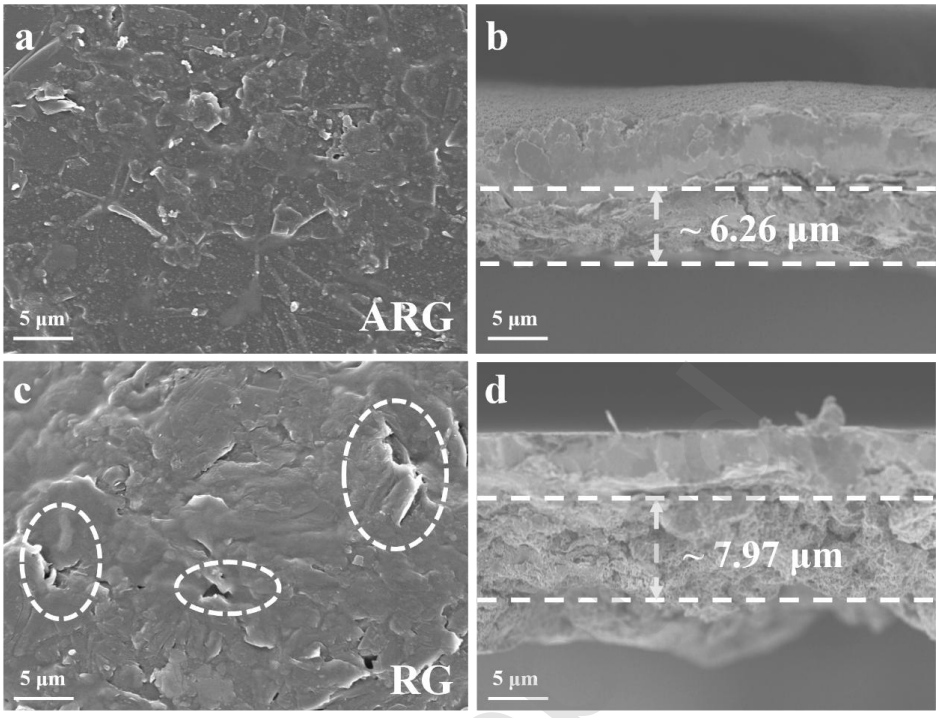


Fig. S25. The surface and cross-sectional SEM images of ARG and RG after 300 cycles at 1C.

Table S1. ICP test results in SG and ARG electrodes.

Samples	Atom Ratio (wt.%)			
	Al	Cu	Li	Mn
SG	0.0147	0.5268	1.7279	0.0566
ARG	1.2764	0.0320	0.0290	0.0047

Just Accepted

Table S2. Comparison of the electrochemical performance of ARG with reported RG anodes.

Material	Rate performance	Capacity retention	Ref.
R-G	320 mAh g^{-1} at 0.2 C	90.4% capacity retention (200 cycles at 0.2 C)	[7]
RG1[#]	328 mAh g^{-1} at 0.1 C 303 mAh g^{-1} at 0.5 C	99.5% capacity retention (100 cycles at 0.1 C) 92.3% capacity retention (500 cycles at 0.5 C)	[8]
RGr	160 mAh g^{-1} at 4 C	73% capacity retention (300 cycles at 4 C)	[9]
PCC-2	324 mAh g^{-1} at 1 C 286 mAh g^{-1} at 2 C	94% capacity retention (250 cycles at 1 C)	[10]
RG-2	321 mAh g^{-1} at 1 C 278 mAh g^{-1} at 2 C	400 cycles at 2 C	[11]
F-RG	350 mAh g^{-1} at 1 C	99% capacity retention (500 cycles at 1 C)	[12]
R-Gra	321 mAh g^{-1} at 0.1 C	~100% capacity retention (100 cycles at 0.1 C)	[13]
PG@PMMA-30	349 mAh g^{-1} at 0.1 C 149 mAh g^{-1} at 1 C	87% capacity retention (500 cycles at 0.1 C)	[14]
DES-G	365 mAh g^{-1} at 0.5 C	95.5% capacity retention (500 cycles at 0.5 C)	[15]
RG2[#]	350 mAh g^{-1} at 0.5 C	96.5% capacity retention (500 cycles at 0.5 C)	[16]
FRA	351 mAh g^{-1} at 0.2 C	95% capacity retention (100 cycles at 0.5 C)	[17]
ARG	366 mAh g^{-1} at 1 C 236 mAh g^{-1} at 4C	98.21% capacity retention (100 cycles at 1C) 75.47% capacity retention (200 cycles at 4C)	This work

Just Accepted

Table S3. Fitted resistances from the Nyquist plots of the ARG, CG, and RG after 3 cycles.

Samples	R_s (ohm)	R_{SEI} (ohm)	R_{ct} (ohm)
ARG	9.84	35.63	90.12
CG	8.91	72.23	99.94
RG	7.05	149.42	178.92

Table S4. The cost analysis of synthetic graphite.

	Dosage	Unit	Unit price		Cost ($)	Data source
Needle coke	0.82	kg	1.3	$/kg	1.07	SMM
Tar pitch	0.2	kg	1.03	$/ kg	0.2	SMM
Energy	136	MJ	0.2	$/kWh	7.56	GPP
Water	2	gal	0.2	$/ gal	0.4	BD
		Total ($/kg)			9.23	

Note: Coal pitch and needle coke are used as precursors to synthesize graphite. The first heating stage is the carbonization process, which takes place at approximately 1573 K for 40 hours, producing a carbon intermediate with defined shape, density, and strength. The second heating stage is dedicated to graphitization, conducted at approximately 3000 K for 10 hours to complete the crystal structure transformation.

SMM: https://www.smm.cn/

GPP: https://www.globalpetrolprices.com/

B2B:https://B2B.baidu.com/

BD: https://www.baidu.com/

Table S5. The cost analysis of pyrometallurgical recycling.

	Dosage	Unit	Unit price		Cost ($)	Data source
Spent anode	2.05	kg	1.1	$/kg	2.26	SMM
Energy	58	MJ	0.2	$/kWh	3.22	GPP
Water	3	gal	0.2	$/ gal	0.6	BD
Ar	5	L	20	$/40L	2.5	B2B
		Total ($/kg)			8.58	

Note: The recycling method employed is pyrometallurgy. The first heating stage is carried out at approximately 673 K for 1 hour to remove the binder through thermal decomposition. Subsequently, flotation and washing processes are performed, consuming 3 gallons of water per unit. The second heating stage is dedicated to the structural repair of the graphite, conducted at 2273 K for 4 hours. An Argon atmosphere is maintained during the high-temperature stage to prevent oxidation.

Just Accepted

Table S6. The cost analysis of hydrometallurgical recycling.

	Dosage	Unit	Unit price		Cost ($)	Data source
Spent anode	1.8	kg	1.1	$/kg	1.98	SMM
Energy	31	MJ	0.2	$/kWh	1.76	GPP
Water	16	gal	0.2	$/ gal	3.2	BD
Acid	2	kg	0.17	$/kg	0.34	SMM
Alkali	2	kg	0.34	$/kg	0.68	B2B
Ar	2	L	20	$/40 L	1	B2B
		Total ($/kg)			8.96	

Notes: In the hydrometallurgical recovery process, the total water consumption is 16 gallons, which includes the flotation process (5.3 gallons of wastewater) and the purification stage (10.7 gallons of wastewater). Chemical treatment involves the use of 2 kg of sulfuric acid and 2 kg of sodium hydroxide to remove impurities. After purification, an Argon atmosphere is employed during the thermal annealing or graphitization stage to restore the crystalline structure of the graphite.

Table S7. The cost analysis of recovered electrodes in our recycling process.

	Dosage	**Unit**	**Unit price**		**Cost ($)**	**Data source**
Spent anode	1.4	kg	1.1	$/kg	1.54	SMM
Energy	18	MJ	0.2	$/kWh	1	GPP
Water	8.6	gal	0.2	$/ gal	1.72	BD
Acid	2	kg	0.17	$/kg	0.34	SMM
NMP	1	kg	1	$/kg	1	B2B
Aluminum nitrate	0.5	kg	0.5	$/kg	0.25	B2B
Ethanol	2	kg	0.6	$/kg	1.2	B2B
Total ($/kg)					7.05	

Notes: ARG production process. Used anode plates are immersed in NMP to recover copper foil, followed by calcination and acid cleaning (total water consumption: 8.6 gal) to purify graphite. RG is dispersed in ethanol, and aluminum nitrate is added to synthesize the precursor. Then, the precursor is heated at 873 K for 3 hours to obtain the ARG material.

Just Accepted

Supplementary references

[1] G. Kresse, J. Hafner, *Phys. Rev. B* **1993**, 47, 558.
[2] G. Kresse, J. Hafner, *Phys. Rev. B* **1994**, 49, 14251.
[3] J. P. Perdew, K. Burke, M. Ernzerhof, *Phys. Rev. Lett* **1996**, 77, 3865.
[4] G. Kresse, D. Joubert, *Phys. Rev. B* **1999**, 59, 1758.
[5] S. Grimme, J. Antony, S. Ehrlich, H. Krieg, *J. Chem. Phys.* **2010**, 132, 154104.
[6] K. Momma, F. Izumi, *J. Appl. Crystallogr.* **2011**, 44, 1272.
[7] J. Chen, R. L. Li, Y. Z. Duan, S. Q. Gong, Y. L. Min, H. X. Li, P. H. Shi, *Green Chem.* **2025**, 27, 9724.
[8] S. Luo, F. R. Liu, Y. Liu, Y. F. Xu, T. Li, Z. Li, P. K. Chu, B. Gao, G. M. Zhou, K. F. Huo, *Adv. Mater* **2025**.
[9] W. Chen, H. T. Qu, R. Y. Shi, J. X. Wang, H. C. Ji, Z. F. Zhuang, J. Ma, D. Tang, J. F. Li, J. Tang, G. J. Ji, X. Xiao, Y. F. Zhu, G. M. Zhou, *ACS Energy Lett.* **2024**, 9, 3505.
[10] B. Wang, Y. Dong, Z. Zeng, H. Lei, Y. Yang, P. Ge, *J. Power Sources* **2024**, 621, 235299.
[11] Z. Yuan, Y. Dong, Z. Zeng, W. Zhao, B. Wang, H. Lei, W. Sun, X. Ji, Y. Yang, P. Ge, *Chem. Eng. J.* **2024**, 491, 151948.
[12] S. Dong, Y. L. Song, K. Ye, J. Yan, G. L. Wang, K. Zhu, D. X. Cao, *Ecomat* **2022**, 4, e12212.
[13] Y. S. Ji, H. Zhang, D. Yang, Y. J. Pan, Z. L. Zhu, X. Q. Qi, X. P. Pi, W. C. Du, Z. H. Cheng, Y. G. Yao, L. Qie, Y. H. Huang, *Adv. Mater* **2024**, 36.
[14] H. Da, S. Pan, J. Li, J. Huang, X. Yuan, H. Dong, J. Liu, H. Zhang, *Energy Storage Mater.* **2023**, 56, 457.
[15] X. Liu, S. Q. Liu, J. H. Pu, R. Zeng, T. Wang, J. S. Meng, J. J. Gaumet, W. Luo, J. W. Liu, *Adv. Sci.* **2025**, 12, e06637.
[16] S. Luo, F. Liu, W. Tianxu, Y. Liu, C. Zhang, C. Bie, M. Liu, P. K. Chu, K. Huo, B. Gao, *Energy Storage Mater.* **2024**, 73, 103833.
[17] W. Y. Chen, R. V. Salvatierra, J. T. Li, C. Kittrell, J. L. Beckham, K. M. Wyss, N. La, P. E. Savas, C. Ge, P. A. Advincula, P. Scotland, L. Eddy, B. Deng, Z. Yuan, J. M. Tour, *Adv. Mater* **2023**, 35.